Article:
Driver, L., Robertson, M.E., Lucas, D.I. et al. (Accepted: 2026) Experimental and Numerical Analysis of Surrogate Optimized de Laval Nozzles in Low-Temperature Supersonic Flows. Physics of Fluids. ISSN: 1070-6631 (In Press)

Experimental and Numerical Analysis of Surrogate Optimized de Laval Nozzles in Low-Temperature Supersonic Flows

Luke Driver,[1] Madeleine E. Robertson,[2] Daniel. I. Lucas,[2] Lok Yiu Wu,[2] Nik Kapur,[3] Dwayne E. Heard,[4] Julia H. Lehman,[2] and Gregory N de Boer[3]
[1)] *School of Computing, University of Leeds, EPSRC CDT in Fluid Dynamics, United Kingdom, Woodhouse Lane, LS2 9JT*
[2)] *School of Chemistry, University of Birmingham, Edgbaston, United Kingdom, B15 2TT*
[3)] *School of Mechanical Engineering, University of Leeds, United Kingdom, LS2 9JT*
[4)] *School of Chemistry, University of Leeds, United Kingdom, LS2 9JT*

(*Electronic mail: G.N.deBoer@leeds.ac.uk)

(Dated: 3 August 2026)

The design of de Laval nozzles for generating low-temperature (7 – 200 K), uniform supersonic jets for chemical kinetics experiments has traditionally relied on the Method of Characteristics (MOC). Our study addresses limitations and sources of unpredictability in conventional MOC-based design by introducing a surrogate based design optimization framework applicable across any CRESU ("Cinétique de Réaction en Écoulement Uniform") apparatus. A free-form geometry parameterization with seven design variables is used to describe the nozzle, and an additional two are used for the operating conditions. The surrogate models are constructed using a global adaptive sampling strategy, enabling accurate prediction of kinetic jet parameters across a wide temperature range of 70 – 130 K. The proposed framework can be used to generate nozzle designs over many operating conditions and constraints, including flow temperature and experimental limitations, capabilities that are not achievable using traditional MOC-based approaches. The optimization of three nozzles reveals a trade-off governing low-temperature supersonic jet formation. Bell-shaped geometries generate supersonic flows that minimize shockwave magnitude across the jet, which are optimal for kinetic studies. The diameter of the isentropic core at the nozzle exit is strongly coupled to flow oscillations. Increasing the core thickness leads to a rapid increase in shockwave magnitude along the jet, while the maximum attainable core thickness decreases with increasing Mach number. The optimized nozzles are experimentally validated, with temperature fluctuations within 1 K of both surrogate predictions and numerical results. These findings demonstrate the coupling between critical parameters for kinetics studies, with implications for CRESU applications.

I. INTRODUCTION

A. Low Temperature Kinetics

The CRESU ("Cinétique de Réaction en Écoulement Uniforme") method is an experimental technique used worldwide to investigate temperature and pressure dependence of the rate coefficient of chemical reactions at low temperatures (< 180 K) that occur in the interstellar medium or atmospheric environments[1–14]. Fundamentally, the CRESU method utilizes an aerodynamic shape known as a de Laval nozzle, which is used to accelerate an inert bath gas (nominally nitrogen, helium or argon at 3000 – 20,000 Pa) and a specified concentration of reactant into a low-pressure vacuum chamber (30 – 300 Pa), which, by energy and mass conservation, generates a low temperature supersonic jet. When combined with bespoke systems, this setup can be used to perform low temperature reaction kinetics. A more detailed description of the approach and its application in low temperature kinetics can be found elsewhere[4,6,9,10,14–19].

B. Nozzle Design, Flow Characterization and Key Parameters

Since the development of the CRESU method, de Laval nozzles have been designed using the Method of Characteristics (MOC) in combination with a viscous boundary layer correction[21–23]. The MOC is used routinely to design an axisymmetric de Laval nozzle profile for a specified set of conditions, such as temperature and bath gas, while ensuring a shock-free exit flow. Nozzles used in the CRESU method typically operate between $1 \leq M \leq 5$, which captures the majority of the temperature range required for routine experiments[3,6,14,24]. However, the MOC is an analytically tractable approach for predicting nozzle characteristics and is only possible as a result of a series of simplifying assumptions to the governing flow equations, including inviscid and isentropic flow. Consequently, (i) it does not accurately predict important global quantities in the supersonic jet that are critical to kinetic studies and (ii) it only produces one de Laval nozzle profile implying that a more optimal profile for kinetics may exist.

The global supersonic jet quantities used in kinetics studies include the average temperature (T_{avg}), which is used as the reaction temperature, the stable flow length (L_{flow}), often referred to as the isentropic core length, which is where the studies of the kinetics of the reactions are performed. A longer jet facilitates the study of slower reactions as the flow length is proportional to the available reaction time (referred to as hydrodynamic time or μ_t)[15], and also allows the use of smaller concentrations of the excess reagents, which can be important in some instances. Another key quantity is the standard deviation of temperature (σ_T) and standard deviation of density (σ_ρ) within the stable flow region. This quantifies the magnitude of the repeated shockwaves in the jet,

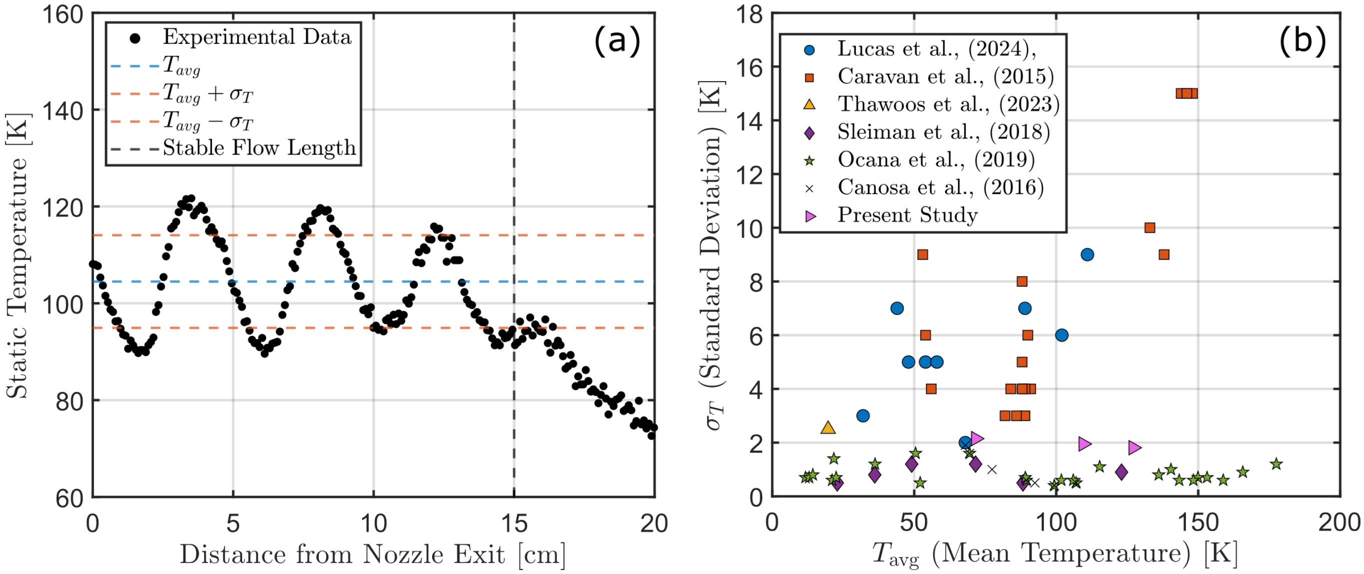

FIG. 1. Example of an axial flow characterization using the Pitot tube approach and the Rayleigh–Pitot equation, which shows the key parameters of the jet, including T_{avg}, σ_T, and L_{flow} (a), and a comparison between σ_T and T_{avg} across the major groups performing pulsed CRESU experiments (b)[4,6,9,17,18,20]. Note this is a selection of groups across the literature, and does not contain every nozzle condition.

where a smaller standard deviation reduces the uncertainty in temperature-dependent kinetic measurements. The σ_T, T_{avg} and L_{flow} of a nozzle designed using the existing MOC method can only be determined once the nozzle is physically manufactured, and its performance may not meet its intended design specification; hence experimental optimization of the operating pressures or a complete redesign of the nozzle is necessary. The existing workflow can be problematic as one nozzle profile and gas is used to generate a discrete temperature for kinetics, hence making many nozzles for temperature or pressure-dependent kinetics using this approach can be costly, time-consuming and tedious. Note that some authors have been able to use gas mixtures to produce a range of temperatures with the same nozzle[4], although experimental optimization and the MOC are still required to design these nozzles.

The performance of a supersonic jet in the CRESU method is normally determined experimentally using a flow characterization technique known as the Pitot tube method[15], and an example with the critical kinetic parameters is shown in Figure 1a. The jet performance of a nozzle designed for a set temperature using the MOC can vary drastically between groups, as shown in Figure 1b, which compares σ_T and T_{avg} across the stable flow length. This is expected to be a result of the differences in nozzle profile, nozzle diameter, gas delivery system (i.e. continuous or pulsed), reservoir volume and reservoir configuration[9,10,25,26]. This therefore indicates the need for a unified nozzle design optimization framework to allow all groups (independent of apparatus) access to well performing nozzles, which aims to improve measurement accuracy for the kinetic research community.

C. Supersonic Flow Modeling

The MOC can be viewed as an accessible, low-fidelity (LF) predictive tool for nozzle design. However, the exponential improvements in computing performance mean that high-fidelity (HF) techniques based on Computational Fluid Dynamics (CFD) are now readily available. The numerical modeling of supersonic jet flows has been carried out and validated rigorously by many authors using Reynolds-Averaged Navier Stokes (RANS) approaches and Large Eddy Simulation (LES) models[27–31]. LES has been shown to be very accurate in predicting experimental results, although this accuracy comes with large computational costs, and is not feasible for a large-scale optimization study. Previous numerical work that is case specific to the CRESU method using steady-state RANS modeling has been rigorously validated against many benchmark nozzles. The results follow general trends and predict global flow quantities (e.g. T_{avg}) to within 5-10% of the experimental results over a range of Mach numbers[32]. More recently, RANS CFD has been utilized to predict the density profile within the reservoir and throat regions, not possible using the Pitot tube approach. This has enabled the calculation of dimer formation of reactants in the jet, which can adversely affect the reaction kinetics by introducing unwanted interactions and side reactions[33].

D. Design Optimization Review

The kinetic performance of a de Laval nozzle depends entirely on the geometric profile, reservoir size, operating pressures, and gases used[32,34]. Shape optimization of de Laval nozzle profiles and operating pressures has been carried out by many authors in the literature across a wide range of application areas. These include surrogate-based modeling, multi objective optimization and adjoint-based methods. The main objectives of these studies are to minimize drag[35] and to maximize thrust[36–41], flow speed[42], pressure recovery[43], and flow uniformity at the nozzle exit[44]. Matsunaga et al. (2022)[45] used a surrogate-based approach to maximize flow uniformity for one specific design Mach number, and showed that it can outperform the MOC for nozzle design. More recently, Kamali et al. (2024)[46] used surrogate modeling to minimize the generation of shock waves across the jet by reducing entropy across the jet axis. However, the objective functions looked at previously are not specific to kinetics and do not consider important properties of the jet, such as L_{flow}, which is much harder to obtain. Existing design optimization studies use parabolic curves and Bezier curves, whereas this study aims to use a free-form geometry approach to generate organic shapes for de Laval nozzle design, which is commonly used in turbine blade and wing design[47–49].

Many of the studies are also typically carried out only for one or a small range of operating conditions or geometry parameters, and in general, studies for de Laval nozzles do not vary these simultaneously across a large design space to understand the underlying trade-offs in governing flow behavior. This is because with large parameter bounds, the convergence of the CFD in many regions in the design space can be difficult or impossible, especially at high Mach numbers where strong shockwaves are present or where the flow is heavily under or overexpanded. This study aims to provide an alternative, novel approach based on dynamic physics-driven design variable bounds to overcome these issues. Most studies that optimize de Laval nozzle profiles focus on objective functions that are readily obtainable, whereas the objective function in this study requires further post-processing of the supersonic jet wake to obtain the kinetic parameters of interest. To the authors' knowledge, this has not been carried out before in the context of de Laval nozzles generally or in the context of kinetics.

Unlike conventional optimization studies, which rely on readily accessible objective functions, the present work considers objective quantities derived from the supersonic jet wake, requiring post-processing to extract the kinetic parameters of interest. This enables direct coupling between nozzle geometry and the fluid-dynamic processes governing low-temperature reaction environments. The key novelty lies in demonstrating that global surrogate models can be used to systematically explore the trade-offs between L_{flow}, σ_{T}, and T_{avg}, while simultaneously revealing the physical constraints imposed by compressible flow dynamics of a de Laval nozzle for a particular CRESU apparatus.

The methodology is applied to the pulsed CRESU apparatus at the University of Birmingham[9], with additional testing at the University of Leeds[10]. While demonstrated in the context of low-temperature kinetics, the framework is general and can be extended to aerodynamic systems where global flow behavior and dynamically constrained design spaces are critical.

This work replaces the traditional MOC design paradigm with a CFD-driven optimization strategy that not only improves nozzle performance, but also provides new physical insight into the coupling between nozzle geometry and supersonic flow performance for kinetic studies.

The paper is organized as follows: Section II details the experimental setup, problem formulation, parameterization, optimization framework, and flow modeling, Section III, shows the surrogate model performance between Kriging and Feed-Forward Neural Networks (FFNN), results from the optimization framework and an experimental validation or the manufactured nozzles. Finally Section IV concludes with recommendations on future application.

II. METHODOLOGY

A. Experimental Apparatus

The experimental pulsed CRESU apparatus used to generate a low-temperature supersonic jet is shown in Figure 2. More information on the exact setup used at the University of Birmingham can be found at Lucas et al.[9].

There are three main features, the first is the cylindrical reservoir which has an internal volume of 30.75 cm^3, where the internal reservoir radius r_{res} and reservoir length L_{res} are 2.30 cm and 1.83 cm, respectively. Two pulsed valves are used to control the flow, where the inlet diameter (d_{in}) of the connection pipe to the reservoir is 0.29 cm. The pulse width and pulse repetition frequency used are 10 ms and 10 Hz, respectively. Crucially, the pulse duration is much longer than the time taken for the jet to reach steady state. The de Laval nozzle can then be threaded onto the reservoir. The reservoir and nozzle assembly is mounted on a translation stage that provides up to 60 cm of travel along the primary axis and $\pm$ 2 cm of movement in both the vertical and spanwise directions, enabling the generation of 2D and 3D contour plots.

The second is the vacuum chamber, which has an internal diameter (d_{chm}) of 40 cm, and a total length of 150 cm, where there are two connected sections allowing easy access to the nozzle and reservoir, which are situated in the main chamber (L_{chm} = 100 cm). The outlet is connected to a vacuum pump, which has a diameter (d_{out}) of 15 cm, and is 87.5 cm from the start of the main vacuum chamber. The pressure in the vacuum chamber is maintained by flowing an ambient slip gas into the chamber, typically nitrogen.

The third is the Pitot tube (with a fast response transducer), which has a leading edge diameter of 3 mm. This is located inside the chamber and is again connected to a separate translation stage for flow characterization, which will be discussed in Section II B. A low temperature environment for kinetics is achieved by pulsing an inert bath gas (nitrogen, helium, or argon) typically at room temperature into the reservoir and then through a de Laval nozzle into a low-pressure (20 – 300 Pa) vacuum chamber. The gas expands and cools through the nozzle, forming a low-temperature supersonic jet that extends tens of centimeters from the nozzle exit, where chemical kinetics can be measured. For the interested reader, more information on kinetic studies can be found at[4,9,10,15].

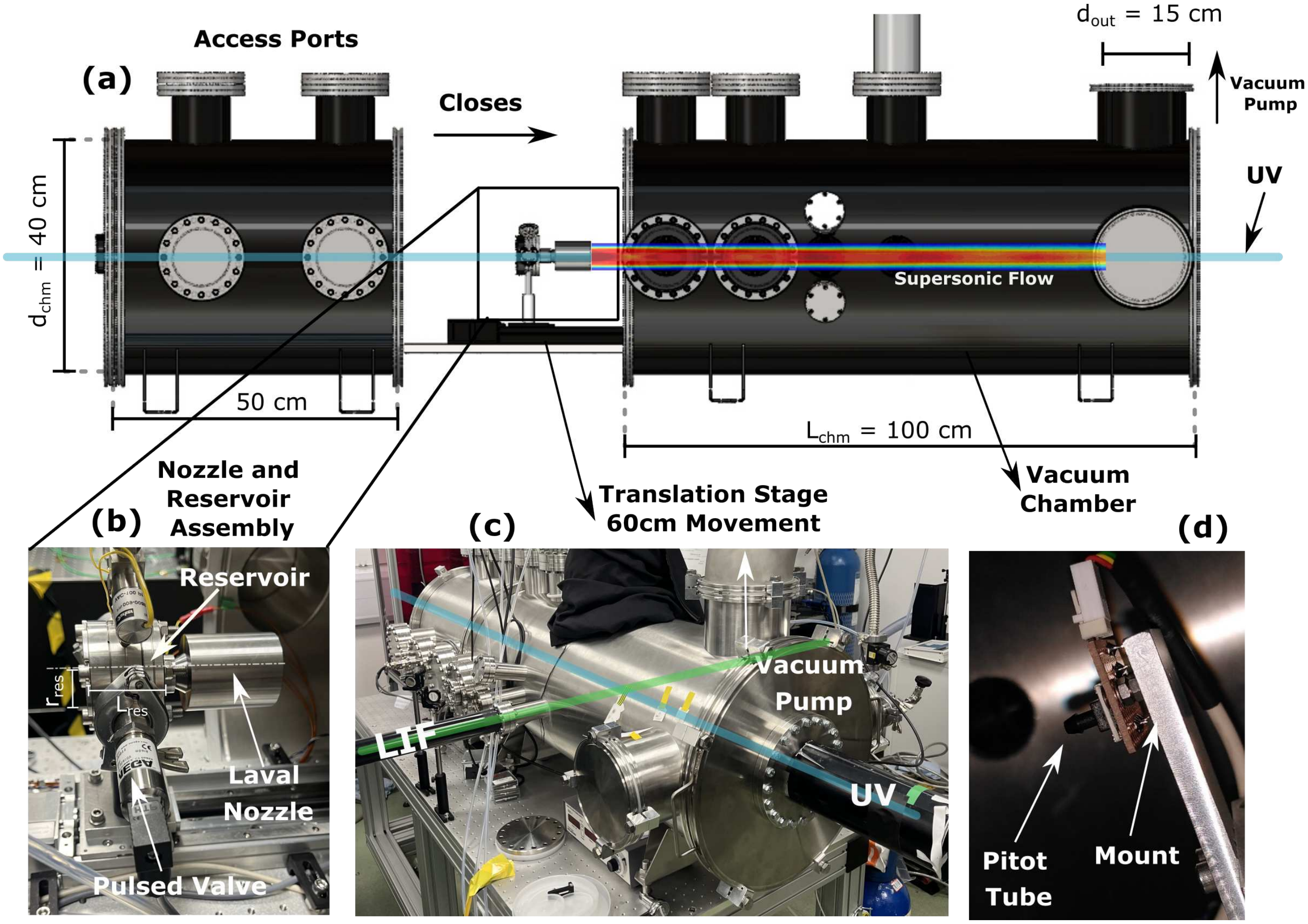

FIG. 2. CRESU apparatus at the University of Birmingham, where (a) is a CAD drawing of the apparatus with key dimensions and labels, with an example supersonic jet (not to scale), (b) is a picture of the Laval nozzle and mounting system, (c) is the vacuum chamber, and (d) is the Pitot tube used for flow characterization. The green region corresponds to the laser induced fluorescence (LIF) beam used for kinetics, and the ultraviolet (UV) beam in blue is used to initiate reactions down the length of the supersonic jet.

B. Experimental Flow Characterization

The experimental method of flow characterization and the important flow quantities need to be outlined to understand their importance in the context of kinetics, which will aid in the formulation of the optimization problem.

The main experimental method used for flow characterization in the CRESU method is known as the Pitot tube method and is used by many groups worldwide[4,9,10,25,26]. Once a nozzle profile has been designed, it is machined using Computer Numerical Control (CNC) out of steel or aluminum on a lathe with a tolerance of $\pm$ 0.1 mm. Once the nozzle has been manufactured, it is then mounted to the reservoir block as shown in Figure 2b. Note that for rapid prototyping 3D printing is used in the field[50], although to avoid surface roughness effects and geometric inconsistencies with the design, CNC manufacturing was used in this study.

To characterize the kinetic performance (i.e. σ_T, L_{flow} and T_{avg}) for a particular nozzle profile and bath gas, first, the chamber pressure and reservoir pressure need to be set. For this particular study, only nitrogen was used as the bath gas. Once the pressures are set, the Pitot tube is laser aligned with the centerline of the nozzle. The Pitot tube (or nozzle and reservoir block depending on the group) is connected to a translation stage as shown in Figure 2b-d, and can be moved in small intervals away from the nozzle exit ($x = 0\,\text{cm}$) across the chamber using a stepper motor. The number of repeats for each Pitot location is 50, and averaged results are shown in this study, more information regarding measurement accuracy can be found in Lucas et al.,[9].

During a gas pulse, the Pitot tube is used to measure the impact pressure (P_{impact}) once the flow has reached a steady state. There is also a calibrated pressure transducer in the center of the reservoir wall, which is used to measure the reservoir pressure (P_{res}) during each gas pulse. The Mach number at the Pitot tube leading edge can then be found using the Rayleigh–Pitot equation:

$$\frac{P_{\text{impact}}}{P_{\text{res}}} = \left(\frac{(\gamma+1)M^2}{(\gamma-1)M^2+2}\right)^{\frac{\gamma}{\gamma-1}} \left(\frac{\gamma+1}{2\gamma M^2-\gamma+1}\right)^{\frac{1}{\gamma-1}} \tag{1}$$

where M is the Mach number, and γ is the ratio of specific heat capacity ($\gamma = 7/5$ for diatomic gases and $\gamma = 5/3$ for monoatomic) for the bath gas that is used during characterization. The corresponding pointwise temperature, pressure and density of the jet can be found using the adiabatic relationships, where the reservoir temperature is taken to be 293 K[9]. The impact pressure across the entire jet can then be obtained by moving the nozzle or Pitot tube relative to each other.

A typical experimental characterization of the jet temperature obtained from this method is shown in Figure 1a. The sinusoidal nature of the temperature profile is a result of shockwave formation and the interaction of these shockwaves with the shear layer. Downstream of the nozzle exit, a growing mixing layer forms, which is due to viscous shearing. The end of the stable flow region is where viscosity dominates the flow, causing the stable region to break. It is important to note that the Rayleigh–Pitot equation is invalid outside the isentropic core region due to inviscid and irrotational assumptions in the analytical derivation, which describes why the experimental data tends towards zero when the flow breaks down. In reality, the temperature rises as it mixes with the ambient gas in the chamber[32]. The global quantities, such as σ_T and T_{avg} are then calculated between the nozzle exit ($x = 0$ cm) and the stable flow length ($x = L_{\text{flow}}$) and are used to infer the performance of the jet. The optimal pressure conditions for a particular nozzle profile, assuming the stable flow length is of an appropriate length to perform kinetics (typically $L_{\text{flow}} > 13 - 15$ cm), are those with the lowest value of σ_T. This provides the lowest uncertainty in the reported reaction rate coefficients for kinetic studies. For all of the experimental characterizations in this study, nitrogen (99.998% BOC) was used, with no additional reactants.

C. Objective Function Formulation

Obtaining L_{flow} from a supersonic flow simulation where the Mach number and flow regimes change drastically is nontrivial, therefore a novel method has been established as part of this study. Typically, the isentropic core length ($L_{\text{flow},1}$) can be defined by using:

$$L_{\text{flow},1} \;=\; \arg\max_{x}\,(kM_{\text{exit}})\Big|_{x=0}^{x=L_{\text{chm}}} \tag{2}$$

where k is a scaling parameter typically between 0.90 – 0.98 and M_{exit} is the Mach number at the nozzle exit[51,52]. The flow length is defined as the furthest point along the Mach number profile across the flow axis, away from the nozzle exit ($x = 0$), that corresponds to kM_{exit}. In this study, 0.95 was chosen as the criterion as it lies in the middle of the typical ranges taken in the literature. Examples of axial Mach profiles are given in Figure 3.

The first criterion in Equation 2 underestimates the isentropic core length significantly for dissipative jets, or if shocks are present at the nozzle exit. To overcome this, k could be reduced but it would drastically overestimate L_{flow} for all other jets, reducing surrogate model quality. To more accurately capture L_{flow}, the location of each local maxima of Mach number across the jet axis is calculated, where:

$$\begin{aligned}
&L_{\text{flow},2} \;=\; \arg\max_{x} M(x)\Big|_{x=0}^{x=L_{\text{chm}}} \\
&\text{such that}\quad f'(x) = \frac{d}{dx}\big(M(x)^m\big) = 0, \\
&f''(x) = \frac{d^2}{dx^2}\big(M(x)^m\big) < 0. \\
&\text{where}\quad |f''(x)| \geq 2
\end{aligned} \tag{3}$$

where the local maxima are calculated from the second derivative of the axial Mach profile, the Mach profile is raised to the power m, where in this case m = 10 to bring out the shocks in the profile closer to the breakdown point (although it can be arbitrarily large). Note that for this criterion to hold, at least two local maxima must exist, as this suggests a sinusoidal jet is generated. Furthermore, if $M < 1$ at the nozzle exit, the flow length is set to be equal to 0 to ensure the flow length for non-supersonic jets is not overpredicted. Both criteria are compared, and the largest length is taken as the stable flow length. Note that if the jet does not contain shocks, the local maxima criterion is not suitable; hence, the development of this hybrid flow length criterion. The standard deviation and average of Mach number, temperature, density and pressure are then calculated in this stable flow region across the jet axis from the nozzle exit to the calculated flow length, and are used in the construction of each surrogate. Alongside axial jet properties, the core thickness at the nozzle exit is also calculated via:

$$r_{\text{core}} = r_{\text{exit}} - \delta_{95} = r_{\text{exit}} - y|_{0.95u_{\text{e}}} \tag{4}$$

where δ_{95} is the boundary layer thickness (taken in this particular case to be 95% of the freestream velocity at the nozzle axis), r_{exit} is the nozzle exit radius, y is the wall normal direction from the flow axis at the nozzle exit, and u_{e} is the exit velocity at the nozzle exit. This formulation of the objective and constraint function may introduce some artificial noise, especially with the approximation of L_{flow}, resulting in the use of regression Kriging and regression FFNNs for this particular application.

D. Design Variables and Parameterization

The de Laval nozzle profile is defined using a NURBS (Non-Uniform Rational B-Spline) curve, which is a free-form deformation (FFD) approach used to generate organic shapes. More information can be found in Piegl & Tiller (1997)[48]. NURBS is commonly used in shape optimization for aerodynamics, including turbine blades, hence its use here. The FFD approach has been used over traditional-based parametrization (i.e. based on physical quantities such as angles) as fewer design variables can be used to achieve a wide range of shapes, hence reducing the problem dimensionality. The

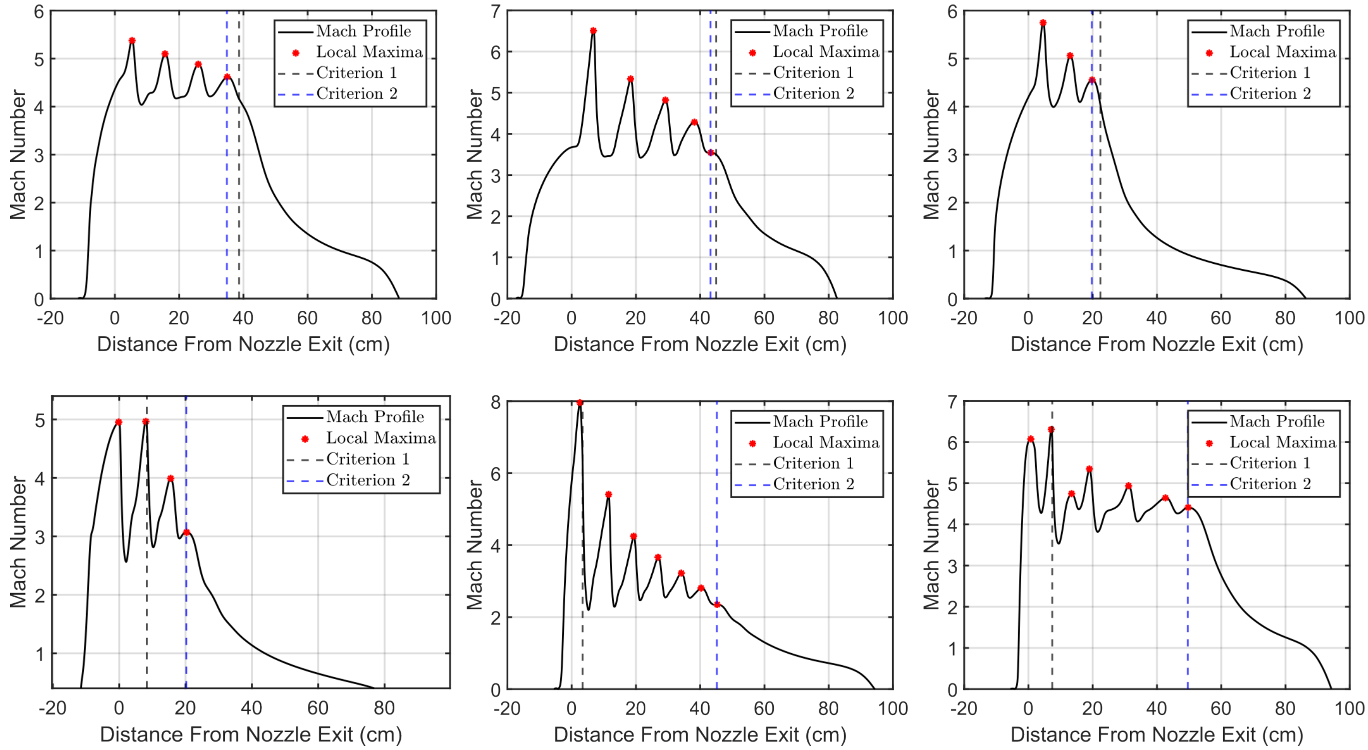

FIG. 3. Comparison between the stable flow length obtained with $L_{\text{flow},1}$ (black dotted line) and $L_{\text{flow},2}$ (blue dotted line) across a variety of different axial Mach number profiles. The red points relate to the local maxima across the axial Mach profile. The distance past the nozzle exit is greater than zero, and negative distances relate to the Mach number inside the reservoir. Note that the Mach profiles are taken at random from the design matrix in Section III.

NURBS curve in this study is calculated using the NURBS MATLAB Toolbox[53,54]. A NURBS curve can be defined as:

$$C(u) = \sum_{i=1}^{k} CP_i N_{i,n}(u) \tag{5}$$

where k is the number of control points CP_i and $N_{i,n}(u)$ are the b-spline basis functions used to construct the curve, where i is the i^{th} control point and n is the degree of the function. The basis functions can be constructed using:

$$N_{i,n}(u) = \frac{u - k_i}{k_{i+n} - k_i} N_{i,n-1} + \frac{k_{i+1+n} - u}{k_{i+1+n} - k_{i+1}} N_{i+1,n-1} \tag{6}$$

where k_i relates to the i^{th} knot in the knot vector. The shape is controlled using a set of four control points denoted "CP", which are $CP_1 = (0, x_1)$, $CP_2 = (x_2, x_3)$, $CP_3 = (x_4, x_5)$ and $CP_4 = (x_6, x_7)$ as shown in Figure 4.

The knot vector can be chosen arbitrarily and has been defined as $k = [0, 0, 0, 0.2, 1, 1, 1]$, ensuring CP_1 and CP_4 are the end points of the curve[48]. Note that the weight term w typically found in this formulation is removed as the weights are kept constant. Only four points are chosen as this is the minimum number of control points required to define the converging section, throat and diverging section of a de Laval nozzle. The control points can either move horizontally or vertically to alter the shape of the curve as indicated in Figure 4.

CP_1 controls the nozzle inlet radius, CP_2 controls the nozzle throat radius and position of the throat relative to the inlet, CP_3 controls the curvature of the nozzle in the diverging section and CP_4 controls the exit radius and length of the nozzle. This results in seven design variables for the de Laval nozzle shape. There are also two more variables, which are the reservoir and chamber pressures, associated with the inlet and outlet pressure boundary conditions of the numerical model which is discussed in Section II G. This results in a nine dimensional optimization problem where the design vector $\mathbf{x} = [x_1, x_2, x_3, x_4, x_5, x_6, x_7, x_8, x_9]$. The upper and lower bound of each design variable are kept between 0 and 1 during the creation of the surrogate model and the optimization process. The design variables are scaled based on the design bounds when they are used in the generation of the nozzle shape and setting of pressures in the numerical setup. The upper and lower bound of each design variable is shown in Table I, and will be now discussed in detail.

Exploring a large design space for a de Laval nozzle where geometric and pressure parameters are heavily coupled can be achieved by using "physics-driven dynamic bounds" developed in this study. This approach narrows down the design space by constraining the design bounds using quasi-1D analytical nozzle equations (see supplementary material) which provide quick approximations to flow properties at the nozzle exit. Based on the 1D approximations, the exit Mach number (and temperature) is dependent on the area ratio (AR) between

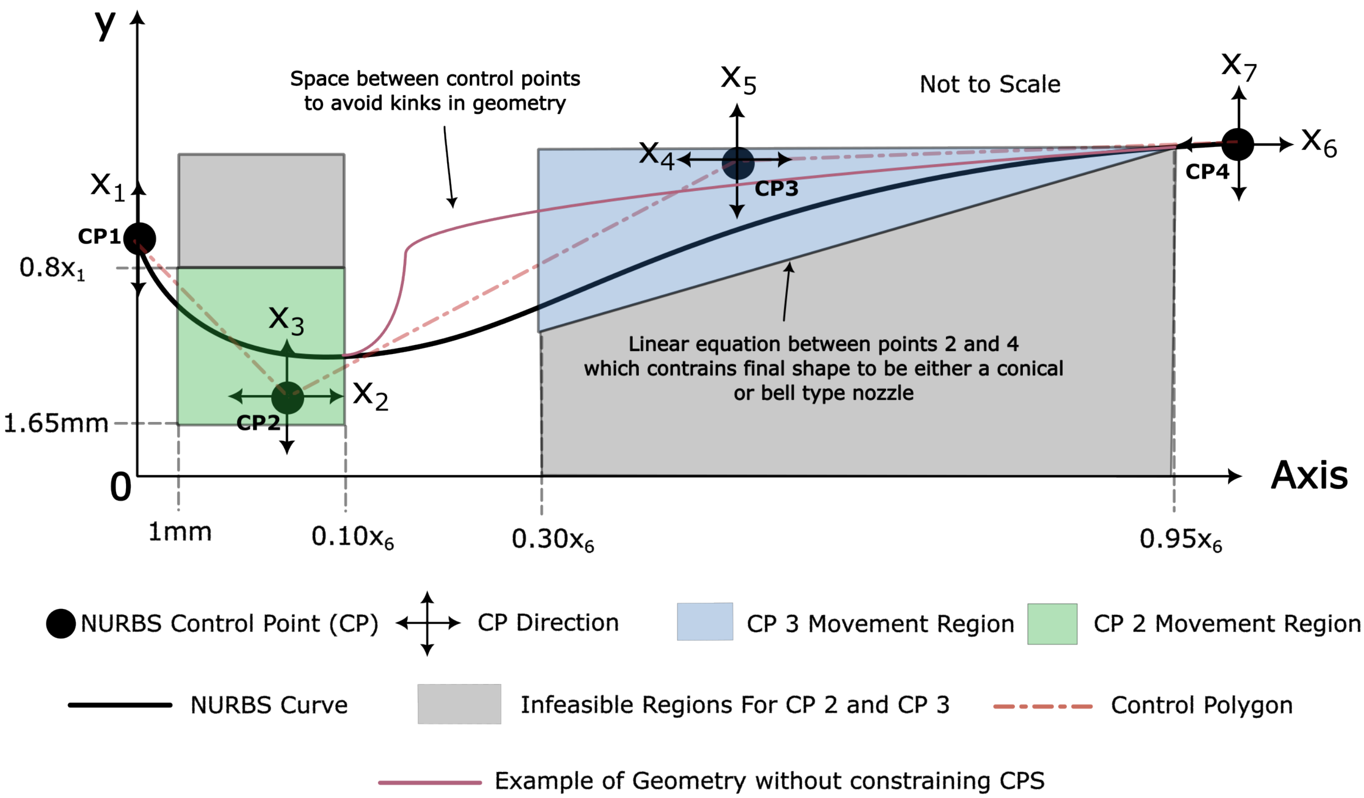

FIG. 4. Parameterization of the de Laval nozzle shape, showing the NURBS control points and their respective movement across the design space.

the throat and nozzle exit and the pressure ratio between the reservoir and chamber. In this example, the nozzle inlet radius (x_1), nozzle length (x_6) and the nozzle throat (x_3) are used to scale the remaining geometric parameters dynamically.

The lower bound of x_6 is based on having sufficient material for the reservoir mount (5 mm), and the upper bound is set to 150 mm. The lower bound of x_3 is chosen to allow the laser to pass through the nozzle for chemical kinetics; any smaller and it could ablate the material or cause laser back-scattering. The upper bound is set so that it is smaller than the lower bound of x_1 to enforce the creation of a converging section.

The lower bound of the nozzle exit radius (x_7) is based on the nozzle throat radius plus a small amount to ensure that the diverging section is slightly larger than the throat. This ensures that the flow accelerates past the sonic point and creates a supersonic flow at the nozzle exit. The upper bound of x_7 was chosen as this is equivalent to the area ratio required to achieve a maximum Mach number of 5 using the analytical nozzle equation with nitrogen as a gas ($\gamma = 7/5$). Note that an additional 4 mm is added to this bound as the CP_2 does not lie exactly on the throat. Dynamically changing the exit radius this way creates nozzle geometries at the same Mach number with different throat and exit radii.

The upper and lower bound of x_2 is chosen so that the throat lies between 1 mm from the nozzle inlet and 10% nozzle length as the diverging section is typically much longer than the converging section.

The lower bound of x_4 is set to 30% of the nozzle length,

TABLE I. Upper and lower bounds of design variables with corresponding units. The value of $PR_{\text{isentropic}}$ is calculated as shown in the supplementary material, where the chamber pressure is equal to x_9. The expression $AR(5, 1.4)$ is the area ratio required to achieve a Mach 5 nozzle, and is shown in the supplementary material. The design variables here relate to the control points shown in Figure 4 used to create the NURBS curve.

Design Variable	Lower Bound	Upper Bound	Units
x_1	4	6	mm
x_2	1	$0.10x_6$	mm
x_3	1.65	$0.8x_1$	mm
x_4	$0.30x_6$	$0.95x_6$	mm
x_5	$\left(\frac{x_7-x_3}{x_6-x_2}\right)x_4 + x_7 - \left(\frac{x_7-x_3}{x_6-x_2}\right)x_6$	x_7	mm
x_6	32	150	mm
x_7	$x_3 + 0.02$	$\sqrt{AR(5,1.4)}x_3 + 4$	mm
x_8	$(1+0.2PR_{\text{isentropic}})x_9$	$(PR_{\text{isentropic}})x_9$	Pa
x_9	20	300	Pa

which is used to ensure that there are no kinks in the nozzle profile. Kinks in the geometry can generate shockwaves and flow separation inside the nozzle, and needs to be avoided at all costs due to its impact on kinetic performance. The lower bound of x_5 is set based on the line equation ($y = mx + c$) between CP_2 and CP_4, this ensures that the nozzle is either conical or bell shaped. If this point is below this line (as shown in Figure 4) it generates poorly performing nozzles, and has been tested and can be seen in the supplementary material. The upper bound has been set to the nozzle exit radius, as placing the point past the exit radius does not generate nozzle-like geometries.

The upper and lower bounds of the chamber pressure (x_9) are set based on the pumping capacity of the vacuum pumps used in the experimental method. The bounds of the reservoir pressure (x_8) are scaled based on the chamber pressure. Once the nozzle has been made, the isentropic equation (see Supplementary material) can be used to approximate the isentropic pressure ratio ($PR_{\text{isentropic}}$) required to run the nozzle. This pressure ratio will always be higher than required, as it assumes 1D, inviscid isentropic flow, and can be used to scale the range of the reservoir pressure based on the area ratio of the nozzle. This dynamic bound also reduces the chance of convergence issues when using large pressure ratios with smaller area ratio nozzles.

E. Problem Formulation

The optimization formulation to improve de Laval nozzles for chemical kinetic studies is a constrained single objective optimization problem with nine design variables, in which σ_T is minimized, and is defined in Equation 7, where $\mathbf{x} = [x_1, x_2, ..., x_d]^T$ is the design variable vector, d is the number of design dimensions (nine in this case), $\mathbf{x}_{\text{lb}}$ and $\mathbf{x}_{\text{ub}}$ are the lower and upper bound of the design variables respectively and $\mathbf{g}$ refers to an inequality constraint. Note that the numerical constraints are based on the experimental apparatus at the University of Birmingham, although they can be adapted for other CRESU setups easily.

$$
\begin{aligned}
& \mathbf{x} = [x_1, x_2, ..., x_9]^n \quad \text{where, } n = 1, 2, ...N \\
\textbf{Minimize} \quad & f(\mathbf{x}) = \sigma_T(\mathbf{x}) \\
\textbf{Subject to} \quad & g_1(\mathbf{x}) = 13\,\text{cm} - L_{\text{flow}}(\mathbf{x}) \leq 0 \\
& g_2(\mathbf{x}) = r_{\text{nozzle}}(\mathbf{x})|_{x=19\,\text{mm}} - 7\,mm \leq 0 \\
& g_3(\mathbf{x}) = r_{\text{nozzle}}(\mathbf{x})|_{x=27\,\text{mm}} - 11\,mm \leq 0 \\
& g_4(\mathbf{x}) = T_{avg,target} - (T_{\text{avg}} + 2) \leq 0 \\
& g_5(\mathbf{x}) = (T_{\text{avg}} - 2) - T_{avg,target} \leq 0 \\
& g_6(\mathbf{x}) = (r_{\text{core}}/r_{\text{exit}}) - (r_{\text{core,target}}/r_{\text{exit}} + 0.02) \leq 0 \\
& g_7(\mathbf{x}) = (r_{\text{core,target}}/r_{\text{exit}} - 0.02) - (r_{\text{core}}/r_{\text{exit}}) \leq 0 \\
& g_8(\mathbf{x}) = x_8 - 5500\,\text{Pa} \leq 0 \\
& g_9(\mathbf{x}) = x_9 - 150\,\text{Pa} \leq 0 \\
\textbf{where} \quad & \mathbf{x}_{\text{lb}} \leq \mathbf{x} \leq \mathbf{x}_{\text{ub}}
\end{aligned} \tag{7}
$$

The inequality constraint g_1 is set to ensure L_{flow} is greater than $L_{\text{flow-target}}$ which can be set based on kinetic requirements, g_2 and g_3 are to ensure that the nozzle fits in the reservoir block and can be mounted, g_4 and g_5 are used to search for a nozzle at a particular target temperature, with a range of $\pm$ 2 K. Similarly g_6 and g_7 are used to target a particular core thickness with respect to the nozzle exit radius and g_8 and g_9 are set based on the typical operating pressures used in the experimental apparatus at Birmingham. Note that many other nozzles exist at operating conditions outside the constrained range used here.

To search for different nozzles across the temperature space that kinetics are performed, $T_{\text{avg,target}}$ can be varied, and the properties of the jet can be controlled by varying L_{flow} and r_{core}. The location of the optimal nozzle in the design space will be defined using $\mathbf{x}^*$, where a superscript $*$ indicates a feasible optimal solution that minimizes the objective function subject to the constraints specified in Equation 7.

F. Optimization Framework

The optimization framework, as shown in Figure 5, uses a mixed fidelity surrogate-based adaptive sampling optimization technique to design de Laval nozzles.

The process starts with an initial Design of Experiments (DoE) with 180 starting sample points ($20d$, where d = 9). These are placed using an optimal Latin hypercube (OLHC), which uses the Φ_q criterion[55] to ensure optimal space-filling properties for the sample points $\mathbf{x}$ across the design (see supplementary material). The initial set of sample points is run through the CFD solver using an LF mesh (see Section II G), and the jet is post-processed to obtain T_{avg}, M_{avg}, σ_T and r_{core}. To ensure robust construction of each surrogate model, all CFD cases were examined for convergence, and any non-converged solutions that could bias the surrogate were excluded (see Section II F 2). Regression Kriging with the Matern52 correlation model is used to create a metamodel for each function (see supplementary material). The surrogate model performance is evaluated against an independent test set of 360 ($40d$) points, again spaced using OLHC, to obtain global performance metrics (see Section II F 3). If the performance does not meet the required accuracy, additional sample points are placed using exploratory adaptive sampling (see Section II F 1) iteratively until the termination criterion is met (see Section II F 4). Note that initially the surrogate models were built with regression Kriging, and later FFNN's were applied on the final data set for comparison.

Once the final surrogate is built, it is then globally optimized using a genetic algorithm (GA), with a small population of 50 to search the design space for possible optimal regions, and then a gradient descent (2500 maximum function calls) is used to fine-tune the location. Note that GA and the *fmincon* function with default options were used from MATLAB. The optimization loop is carried out 40 times to ensure a robust search of the design space. The top ten candidate designs are first evaluated using a LF mesh. The three candidates that minimize the objective function are then re-evaluated with a HF mesh, and the design exhibiting the best performance with respect to σ_T is selected. Once the optimal nozzle and pressure conditions are found, the nozzle can be manufactured and tested to validate the numerical framework. Detailed information of the steps highlighted in Figure 5 can be found in the following sections or supplementary material.

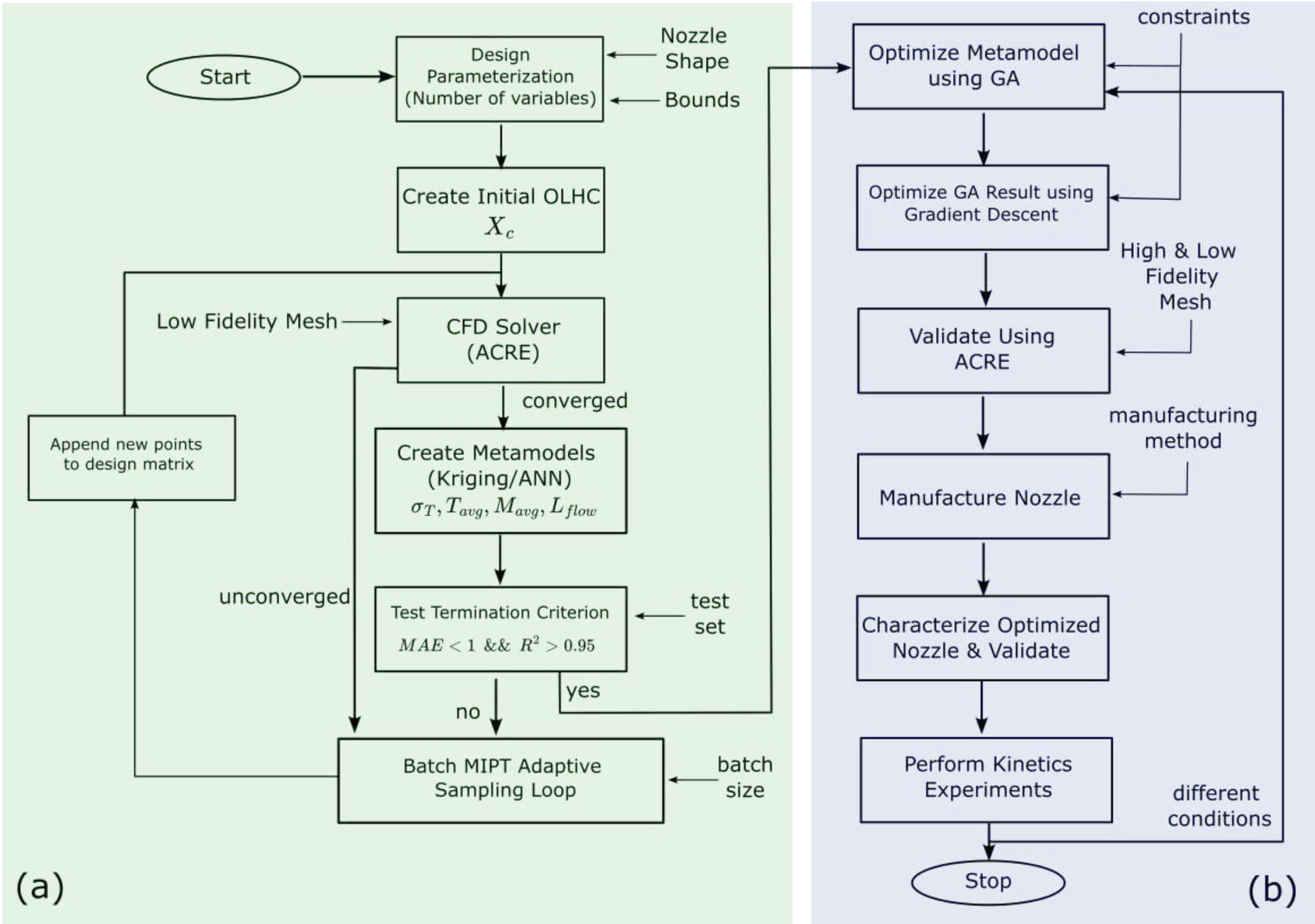

FIG. 5. High level overview of the optimization framework which uses regression Kriging and a global exploration adaptive sampling method. The highlighted green region shows the creation of the Kriging model and the adaptive sampling process, and the blue region shows how the model is optimized to generate a profile and conditions which can be manufactured to perform reaction kinetics. GA refers to the optimization search known as a genetic algorithm.

1. Adaptive Sampling Method

Depending on the current constraints (e.g $T_{\text{avg-target}}$), the optimal nozzle can be anywhere in the design space, hence a globally accurate model is required for this particular application. The two main types of global exploration method are either distance based or variance based[56,57]. Variance based methods use s^2, which is available directly from the Kriging model, although they are prone to heavy clustering on the design bounds where variance is large[58]. Distance based methods alleviate problems of clustering and provide full global coverage of the design space. In particular, an adaptation of the Monte-Carlo-Intersite-proj-th (MIPT) method will be used based on its ability to provide global accuracy and ease of implementation[59]. Additional points are added based on the existing points in the design space. A new point is placed the furthest away from existing points by maximizing:

$$x^{n+1} = \arg\max_{x^* \in \mathscr{C}} \left(\min_{x \in \mathscr{X}} \|x^* - x\| \right) \tag{8}$$

where x^{n+1} is a new point, $\|x^* - x\|$ refers to the Euclidean distance between a candidate point (x^*) and all existing points (x). The computational cost of MIPT scales with both problem dimensionality and a large number of candidate points, which is required for good design space coverage. Instead of finding a new point using Monte-Carlo sampling, a genetic algorithm is used to efficiently search the design space for the best candidate point. The closest point (based on Euclidean distance) in the existing data set to the candidate point is calculated using the k-nearest-neighbor search method in MATLAB. The starting batch size chosen was 360 (equivalent to $40d$). The new design points are passed to the CFD solver sequentially, but can be readily run in parallel with the appropriate computing resources. The adaptive sampling continues until the $MAE < 0.5$ and $R^2 > 0.95$ for the σ_T model. The termination criterion can be reduced, although with significantly larger cost.

Many adaptive sampling algorithms are sequential, requiring a Kriging model update every iteration. This process can become expensive, as the computation required for a Kriging model scales with $O(n^3)$[60]. The proposed method eliminates the need for Kriging information at every step. Instead, the next design point can be treated as a pseudo-point and added to a fictitious design matrix. This allows a batch of new sample points to be calculated and passed through to the ACRE framework. This significantly reduces compute time to build the model and is proportional to the batch size of new samples.

2. Convergence Handling

Non-converging CFD cases are inevitable when exploring a large design space, especially on the variable bounds; proper handling of these cases is crucial to ensure a smooth model-building process. To ensure a supersonic flow converges, two parameters of interest can be investigated: the maximum Mach number at the flow axis, relating to the largest shock, and the difference in mass flux between the inlet and outlet boundaries. The mass flux convergence criterion for a converged case is calculated as:

$$conv_1 = abs((\dot{m}_{\text{out}} - \dot{m}_{\text{in}})/\dot{m}_{\text{out}}) < 0.02 \tag{9}$$

where $\dot{m}_{\text{in}}$ and $\dot{m}_{\text{out}}$ relate to the mass flux at the inlet and outlet boundary, and the maximum acceptance threshold of 2% was applied to prevent overly restrictive convergence criteria and to retain cases with minor deviations. The second criterion based on the maximum axial Mach number is:

$$conv_2 = ((M_{\max,i+1} - M_{\max,i}) - \sum_{i=1}^{50} \frac{M_{\max,i}}{50}) / \sum_{i=1}^{50} \frac{M_{\max,i}}{50} < 0.02 \tag{10}$$

where $M_{\max}$ is the maximum Mach number, this criterion is only calculated in the last 50 iterations of the calculation, and $i = 1$ relates to the 50 values before the final iteration. This criterion is also accepted if the value is less than 2%. Both $conv_1$ and $conv_2$ must be $< 2\%$ to be converged. If the solution is not converged, the design point is left in the design matrix during the adaptive sampling scheme as a pseudo point, to ensure it is not run through the CFD again. The Kriging model during the adaptive sampling algorithm is created without these points and the remaining points (assuming there are many more converged than un-converged) are used to approximate the value at a non converged design location.

3. Test Data and Error Metrics

To evaluate the accuracy of each surrogate model, a set of training data points is used to compare against the Kriging and FFNN model that is generated. The error metrics used are the mean average error (MAE), normalized mean average error ($NMAE$) and correlation (R^2) which are calculated using:

$$MAE = \frac{1}{n} \sum_{i=1}^{n} \frac{|Y_i - \hat{Y}_i|}{Y_i} \tag{11}$$

$$NMAE = MAE/(max(Y) - min(Y)) \tag{12}$$

$$R^2 = 1 - \frac{\sum_{i=1}^{n} (Y_i - \hat{Y}_i)^2}{\sum_{i=1}^{n} (Y_i - \bar{Y})^2} \tag{13}$$

where n is the total number of samples, Y is the true value from the test data and $\hat{Y}$ is the value from the Kriging model. These error measures are also used to compare the accuracy of the Kriging and FFNN approaches. The test set is created using the same OLHC method as in the supplementary material, where $40d$ samples were used to ensure global coverage.

4. Termination Criteria

The termination criterion to stop the adaptive sampling loop uses a hybrid approach. The first criterion is error based, where if $MAE \leq 0.5$ and $R^2 \geq 0.95$ for the σ_T model, the adaptive process stops. The second is based on the value of MAE between consecutive adaptive sampling loops, here five most recent values of MAE of the σ_T model are taken, and if the gradient of the line across these points is < 0.00001, the adaptive sampling stops as the MAE has stabilized, and further points are redundant. Note that only the σ_T model is taken during the adaptive sampling process, as the improvement in MAE and R^2 is comparable across all models with an increase in the number of samples. Also this reduces the computational cost of generating a Kriging model for each design variable and constraint. This behavior was identified from lower dimensional tests.

G. Flow Modeling

The numerical model used here has been described in detail with sensitivity, mesh dependence and validation studies in previous works[32], where the CFD framework utilized in this work can be found at https://github.com/sc1dr/ACRE. A natural progression from this work is to replace the nozzle design using the MOC with an efficient and modern design optimization framework, again using CFD predictions to produce de Laval nozzles that are optimal for chemical kinetics applications. To model high speed compressible flow, the Favre weighted mass, momentum and energy equations are used:

$$\frac{\partial \bar{\rho}}{\partial t} + \frac{\partial}{\partial x_j}(\bar{\rho}\tilde{u_j}) = 0 \tag{14}$$

$$\frac{\partial(\bar{\rho}\tilde{u_i})}{\partial t} + \frac{\partial}{\partial x_j}(\tilde{u_i}\bar{\rho}\tilde{u_j}) = \frac{\partial \bar{P}}{\partial x_i} + \frac{\partial \bar{\sigma}_{ij}}{\partial x_j} + \frac{\partial \tau_{ij}}{\partial x_j} \tag{15}$$

$$\frac{\partial(\bar{\rho}\tilde{E})}{\partial t} + \frac{\partial}{\partial x_j}(\tilde{u_j}\bar{\rho}\tilde{H}) = \frac{\partial}{\partial x_j}\left(\bar{\sigma_{ij}}\tilde{u_i} + \left(\mu + \frac{\tilde{\mu_t}}{\sigma_k}\frac{\partial k}{\partial x_j}\right)\right) - \frac{\partial}{\partial x_j}\left(\frac{c_p\tilde{\mu_t}}{Pr}\frac{\partial \tilde{T}}{\partial x_j} + \frac{c_p\tilde{\mu_t}}{Pr_t}\frac{\partial \tilde{T}}{\partial x_j} + \tilde{u_i}\tau_{ij}\right) \tag{16}$$

where ρ is the fluid density, u_i is the fluid velocity component, P is the fluid pressure, T is temperature, $\bar{\sigma}_{ij}$ is the mean viscous stress, τ_{ij} is the Reynolds stress tensor, μ_t is the turbulent viscosity and k is the turbulent kinetic energy. Variables indicted with overbar ($\bar{\rho}_i$) and tilde ($\tilde{u}_i$, $\tilde{u}_k$) represent the Reynolds-averaged and Favre-averaged quantities respectively. $\tilde{E}$ is mean energy, $\tilde{H}$ is the mean fluid enthalpy. The Prandtl number is defined as $Pr = c_p\mu/\kappa$, where κ is thermal conductivity, and c_p is the specific heat capacity of the fluid at constant pressure. The turbulent Prandtl number Pr_t is set to 0.9. The ideal gas law ($P = \rho RT$) was used as an equation of state, where R is the ideal gas constant. The temperature dependence on viscosity, thermal conductivity and specific heat capacity were modeled by fitting data obtained from NIST (National Institute of Standards and Technology)[61], and pressure dependence on these quantities was neglected. Pure nitrogen was used as the working fluid gas for the computational simulations with no chemical reactions. It is further assumed that gas-phase condensation is unlikely to occur in experiments conducted at temperatures below 70 K, owing to the low collision frequency, collimated flow, and short transit time through the de Laval nozzle.

The turbulence model used to close the Reynolds stress tensor was the $k-\omega$ shear stress transport model, as it has the best performance in determining flow separation and shock-wave interactions when applied to supersonic flows[29,30,32]. The steady-state coupled 2D axisymmetric finite volume solver in Ansys Fluent 2022 R2 was used with a pseudo-transient approach and all flow variables are discretised using second-order gradient schemes. Each case was initialized using the full-multi-grid method with five nested grids to accelerate convergence and ensure a robust initial solution for both subsonic and supersonic cases. All simulation are ran until all residuals are below 1e-5, or a maximum or 2500 iterations, with the majority of simulations converging in under 1500 iterations. The computational domain used for all flow simulations is shown in Figure 6, where the dotted line indicates a symmetry boundary, solid black edges indicate no-slip adiabatic walls. Note that nozzle exit is connected to the chamber wall as done in previous studies[45], although future work could examine the effect of this boundary on the wake. The green and red edges are set to pressure inlet and pressure outlet boundaries, respectively, that act normally, with a temperature of 293 K, (set to ambient lab conditions), and a turbulent intensity of 1%. The exact turbulent conditions on the boundaries are unknown. although minimal dependence on the jet has been shown previously[32]. The outlet edge is scaled based on the equivalent area of the 3D outlet, which in this case its 1.4 cm (where the physical outlet is 15 cm in diameter), although the inlet is kept at 0.29 cm, more information on setup can be found at Driver et al.,[32]. The pressure set at the inlet and outlet boundaries is the total pressure, equivalent to the measured pressures obtained via experiments. The dimensions of the CRESU apparatus are taken from the apparatus at the University of Birmingham[9] and are shown in Figure 6. The vacuum chamber length will change as this depends on the length of the nozzle that is used i.e. having a longer nozzle will decrease the maximum downstream space for the jet wake in the vacuum chamber, identical to the experiments.

The meshing approach utilized in this study is the same as that employed in the previous work by Driver *et al.*[32], but with a significantly lower mesh density (4 times less dense). Preliminary analyses indicate that the overall model trends remain largely consistent between HF and LF meshes. At the same time, the LF cases require only one-tenth of the computational time. This increases the accessibility of the approach by other groups and can be run with different bath gases with minimal effort. A more robust justification of a LF-fidelity mesh approach is given in the supplementary material.

III. RESULTS AND DISCUSSION

To illustrate the applicability of the global modelling approach described in this work, a comparison between the model performance (see Section III A) of regression Kriging and FFNNs for each of the kinetic parameters (σ_T, T_{avg}, L_{flow} and r_{core}) is first discussed. The resulting surrogates were then used to design three nozzles using the same surrogate at three different jet temperatures (see Section III B). The designed nozzles were then validated experimentally using the approach described in Section II B and their performance is compared to the surrogate and CFD predicted flows (see Section III C).

A. Surrogate Model Performance

The original surrogate model was generated using regression Kriging as the model builder in the optimization loop (see Section II), FFNN's were then applied using the final number of design samples obtained using the adaptive framework for comparison. The final surrogate contained 10980 samples, with 57 non-converged cases (typically at design space extremes), equating to 0.5% of the total number of samples. Note the second termination criteria was triggered, meaning that a further increase in the number of design samples resulted in a minimal decrease in model error across five successive batches. The average compute time for a single LF CFD calculations was 4.55 minutes on a 40 Core Xeon 2.0 GHz CPU, resulting in a total wall-clock time of 861 hours. Note that the LF approach also had the advantage of being easier to converge especially in the presence of large shock-waves in comparison to a HF mesh. An equivalent surrogate using a HF meshing approach to obtain a surrogate model at a similar level of accuracy would have taken approximately 8612 hours, hence the adoption of a LF mesh to generate the surrogate in this work (see supplementary material).

Figure 7a-b shows the evolution of MAE and R^2 for each model during the adaptive sampling process using regression Kriging. The model error reduces rapidly across all models until approximately 5000 samples are present in the design space. The error reduction rate then decreases substantially between 5000 – 10000 samples, indicating global trends have been discovered. Although due to the curse of dimensionality, an exponential number of samples is required to decrease the

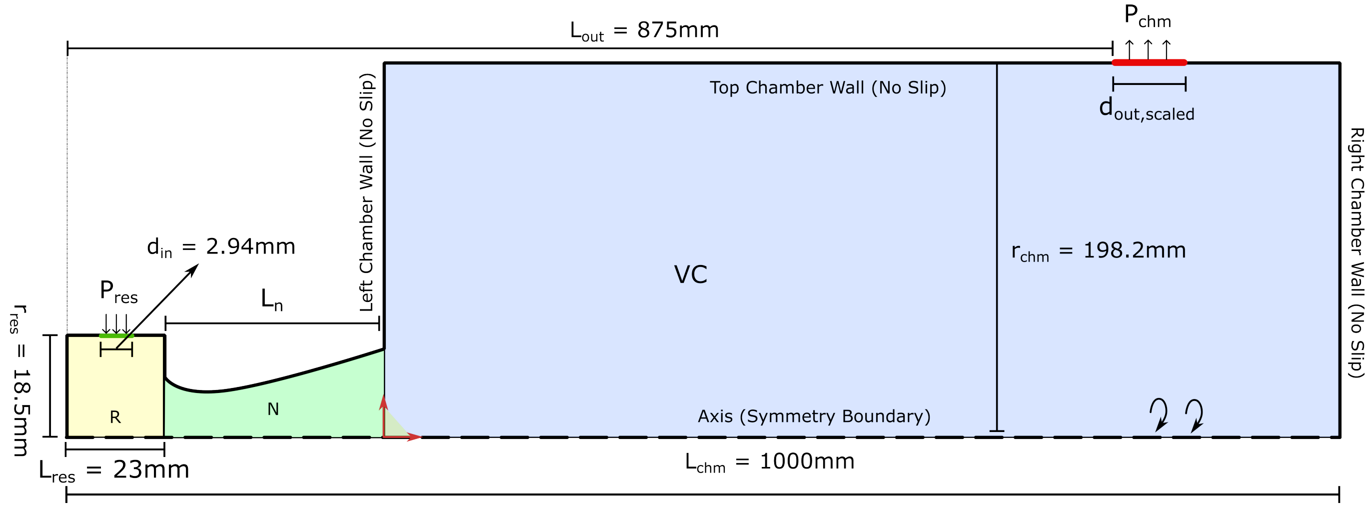

FIG. 6. Computational domain used in CFD calculations with labeled dimensions and sizes. The dimensions are from the CRESU apparatus used at the University of Birmingham. r_{res} is the reservoir radius, L_{res} is the reservoir length, d_{in} is the diameter of the inlet valve connected to the reservoir, L_{chm} is the chamber length, r_{chm} is the chamber radius and L_{out} is the length of the outlet from the edge of the reservoir. $d_{\text{out,scaled}}$ is the scaled outlet boundary. Black lines indicate solid walls, the green and red edges are the pressure inlet and pressure outlet boundaries, respectively, and the dotted line is the axisymmetric boundary. R is the reservoir, N is the nozzle, and VC is the vacuum chamber.

error of the model, hence the slowdown in model error with an increase in sample points.

Figure 7c-f shows a comparison between the predicted CFD values (ground truth) of the identical independent global OLHC test set compared to both the regression Kriging (black) and FFNN (blue) surrogate predictions for the σ_T, T_{avg}, L_{flow} and r_{core} models, respectively. The T_{avg} model ranges from 50 - 300 K using a bath gas of N_2, illustrating the possible temperature range of nozzles that can be designed using this global modeling approach, Samples that lie closer towards $y = x$ line show improved predictive capabilities than the former. The regression Kriging models show good overall predictive capabilities across all models. This highlights its robustness in capturing overall global trends in the data, although it can struggle to capture local variability. This is evident by the larger spread predictions with respect to the $y = x$ line in comparison to the FFNN predictions. The spread away from $y = x$ is more apparent with the σ_T and L_{flow} models, owing to the fact that the design space is complex due to variations in flow regime and Mach number.

A comparison between the performance of both the Kriging and FFNN surrogate is shown in Table II. The standard deviation between the regression Kriging and ground truth predictions for the σ_T, T_{avg}, L_{flow} and r_{core} models is 0.92 K, 1.50 K, 0.71 cm and 0.20 mm, respectively. In comparison, the FFNNs predictions show improved clustering towards $y = x$ across all models, meaning that alongside capturing global trends, the FFNN can accurately capture local variability across the entire design space in comparison to regression Kriging for this particular application. This trend is also seen when comparing the MAE, $NMAE$ and R^2 across all of the models with the Kriging and FFNNs as shown in Table II. Upwards of a 46% reduction in MAE is found across all models when using a FFNN instead of the traditional regression Kriging with a rich dataset. The standard deviation between the ground truth and FFNN surrogate predictions for the σ_T, T_{avg}, L_{flow} and r_{core} models is 0.29 K, 0.60 K, 0.53 cm and 0.06 mm, respectively. Therefore the FFNN shows reduced variability around $y = x$ of 217%, 150%, 34% and 223% for σ_T, T_{avg}, L_{flow} and r_{core} models respectively compared to the regression Kriging model. Furthermore, the Kriging model building process took $\approx$ 30 hours using the final 10980 samples on a 2.0 GHz 40 Core Xeon processor due to Kriging scaling with $O(n^3)$ (where n is number of samples), whilst the FFNN approach only required $\approx$ 5 minutes locally, showing that the FFNN model building approach is 360 times less computationally expensive, whilst improving global accuracy drastically across all models. The RAM requirements for the FFNN are significantly reduced compared to the Kriging model, as the RAM requirement scales with n due to the inverse of a covariance matrix. Note that regression Kriging has been shown to outperform FFNN's with smaller datasets that are typically used in lower dimensional optimization problems. Therefore, the FFNN surrogate is used herein to optimize based on the constraints given in the problem formulation (See Section II).

B. Optimization Results

To evaluate the performance of the global surrogate and optimization approach, $T_{\text{avg,target}}$ = 70 K, 110 K and 130 K were considered using the same FFNN surrogate. Although the surrogate model was originally trained over a broader temperature range of 50–300 K (Figure 7), validation in this work is restricted to the narrower interval of 70–130 K. Nevertheless, it is expected that the surrogate will retain its predictive capability outside this range, as the underlying physical behav-

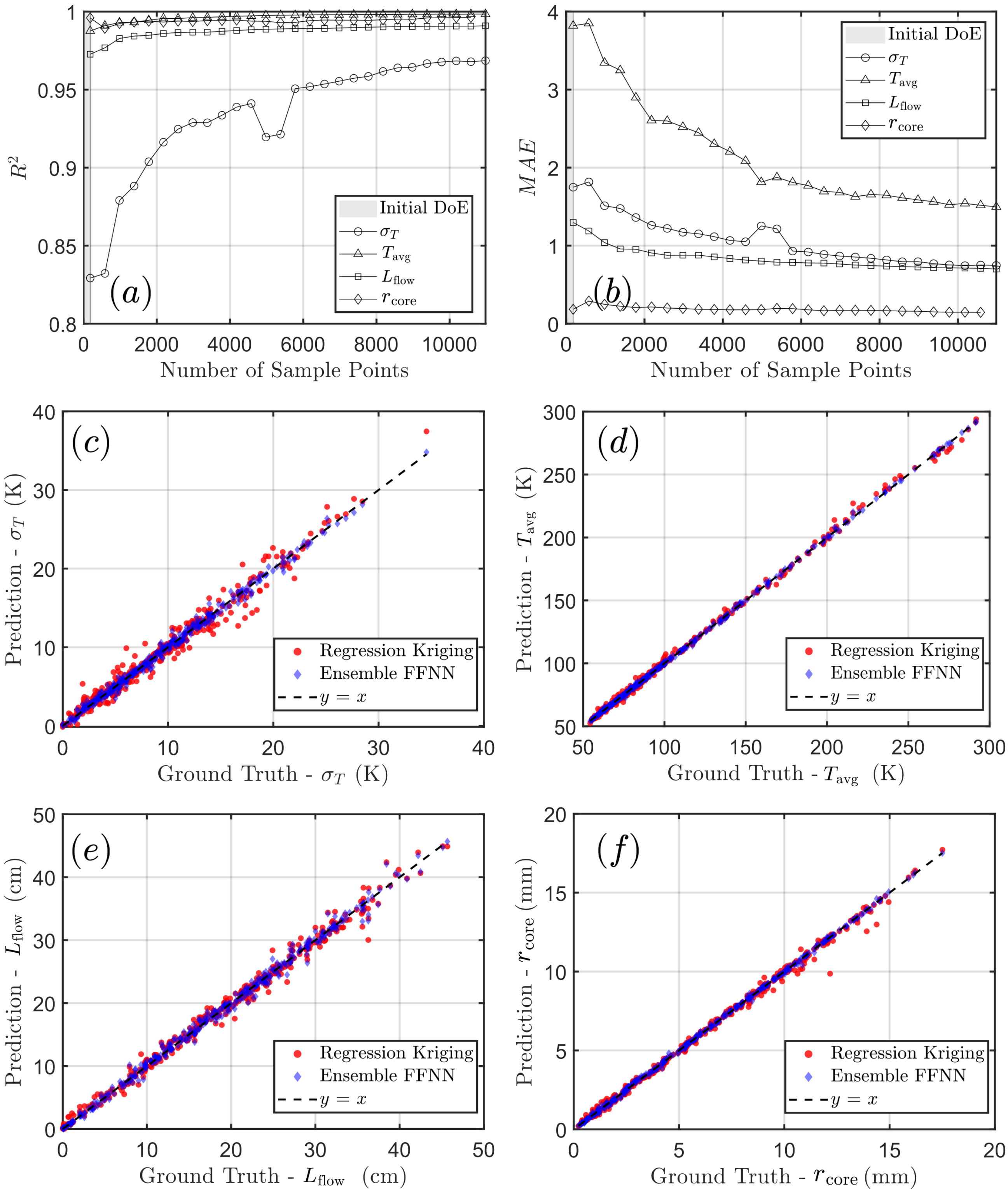

FIG. 7. Evolution of R^2 and MAE during the adaptive sampling for each surrogate model during the Kriging adaptive sampling process are shown in (a) and (b), respectively. Comparison of predictions of Kriging and FFNN models between the independent test set for (c) σ_T, (d) T_{avg}, (e) L_{flow} and (f) r_{core}.

TABLE II. Comparison between model prediction and test set for Kriging and FFNN for each of the surrogates, MAE refers to mean average error, *NMAE* refers to normalized mean average error, normalized by the difference between the maximum and minimum value in the test set for comparison. The compute time for the FFNN was less than 5 minutes locally on a 6 core machine, whilst the Kriging model with 10980 samples took $\approx$ 30 hours. The percentage difference is calculated via $|(a-b)/b|$ between the Kriging and FFNN models. The difference between *NMAE* and *MAE* will be identical, as they are normalized by the same values. The standard deviation σ refers to the variation from of the predicted value from the true value.

Model	Metric	σ_T (K)	T_{avg} (K)	L_{flow} (cm)	r_{core} (mm)
Kriging	MAE	0.7057	1.341	0.7111	0.1456
Kriging	*NMAE*	0.0204	0.0057	0.0156	0.0084
Kriging	R^2	0.9729	0.9987	0.9910	0.9966
Kriging	1σ	0.92	1.50	0.71	0.20
FFNN	MAE	0.3169	0.5738	0.4863	0.0602
FFNN	*NMAE*	0.0092	0.0024	0.0106	0.0035
FFNN	R^2	0.9951	0.9998	0.9954	0.9996
FFNN	1σ	0.29	0.60	0.53	0.06
Difference (%)	MAE	123	134	46	142
Difference (%)	R^2	2.28	0.110	0.444	0.301
Difference (%)	1σ	217	150	34	233

ior remains consistent across nozzles. Furthermore, the CFD framework employed represents a higher-fidelity extension of the MOC, which has been successfully applied across the full temperature range considered.

Before selecting a nozzle geometry to manufacture, however, r_{core} and other experimental design parameters need to be considered. To understand the influence of r_{core} on σ_T, T_{avg} and L_{flow}, a single objective optimization was conducted by varying $r_{\mathrm{core,target}}/r_{\mathrm{exit}}$, from 0.4 to 0.8 in intervals of 0.05 and keeping $T_{\mathrm{avg,target}}$ constant for each nozzle temperature, with the constraints also remaining the same for all runs. The mathematical formulation of the problem is shown in Equation 7.

Figure 8 shows the top ten candidate designs minimizing σ_T, with the gray regions indicating the $\pm 2\%$ tolerance applied to the $r_{\mathrm{core,target}}$ constraint. For the $T_{\mathrm{avg}} = 110$ K and $T_{\mathrm{avg}} = 70$ K cases, similar behavior is observed, whereby σ_T remains approximately constant with increasing core thickness until a critical threshold is reached (0.65 and 0.75, respectively), beyond which a sharp increase in flow oscillations occurs. This behavior is consistent with the onset of an underexpanded regime, where increasing core momentum leads to stronger shock structures due to pressure mismatch between the nozzle exit and the ambient conditions.

At lower $r_{\mathrm{core}}/r_{\mathrm{exit}}$ values, the optimization yields longer nozzles that promote gradual, near-isentropic expansion, resulting in low σ_T. However, the associated boundary layer growth becomes significant relative to the exit radius, reducing the effective uniform core region available for kinetic measurements. This demonstrates a fundamental trade-off between σ_T and usable r_{core} for kinetics. In the absence of the r_{core} constraint, the optimization converges towards low pressure operating conditions. Although the CFD predicts comparable values of L_{flow} and T_{avg} in this regime, the flow exhibits reduced core momentum, resulting in a smaller r_{core}. In these cases, shock formation is suppressed and σ_T remains artificially low. However, experimental testing of such low-pressure designs ($P_{\mathrm{res}} < 2000$ Pa) shows poor agreement with CFD predictions, indicating that these solutions are not physically robust for practical applications for this apparatus due to potential rarefaction effects, where more work is needed to understand this transition (see Supplementary Material).

For the $T_{\mathrm{avg}} = 130$ K case, σ_T exhibits a parabolic dependence on core thickness, with a minimum near 0.65, consistent with the existence of an optimal balance between σ_{T} and r_{core}. This behavior is less apparent at lower temperatures due to the imposed design constraints, but the same underlying trade-off remains. These results demonstrate that minimizing σ_T alone is sufficient for nozzle design, as both T_{avg} and L_{flow} remain relatively insensitive to $r_{\mathrm{core}}/r_{\mathrm{exit}}$ across a wide design space. Instead, the inclusion of a core thickness constraint is necessary to ensure physically meaningful solutions for kinetics, ensuring the largest possible region for kinetic sensing. More generally, the results reveal a coupled relationship between r_{core}, σ_{T}, and L_{flow}, whereby reductions in σ_T are associated with shorter usable flow regions, highlighting an intrinsic trade-off between stability and kinetic sampling volume.

To identify designs that balance L_{flow} and r_{core}, candidate solutions were selected from regions immediately preceding the sharp increase in σ_T. For each temperature, the top ten candidates from these regions were evaluated using LF CFD, followed by HF CFD predictions of the top three best-performing designs. The optimal design for each T_{avg} was taken as the configuration minimizing σ_T while satisfying the core thickness constraint. The surrogate model predictions show strong agreement with CFD, with deviations within 1 K for both σ_T and T_{avg}. Furthermore, comparison between LF and HF CFD demonstrates consistency across all key metrics (σ_T, T_{avg}, L_{flow}, r_{core}), confirming the robustness of the multi-fidelity approach. Minor discrepancies in L_{flow} arise due to under-resolution of boundary layer growth in the LF simulations.

A comparison between the optimal nozzle profiles for each design temperature and axial static temperature profiles of the HF CFD predictions is shown in Figure 9, with the corre-

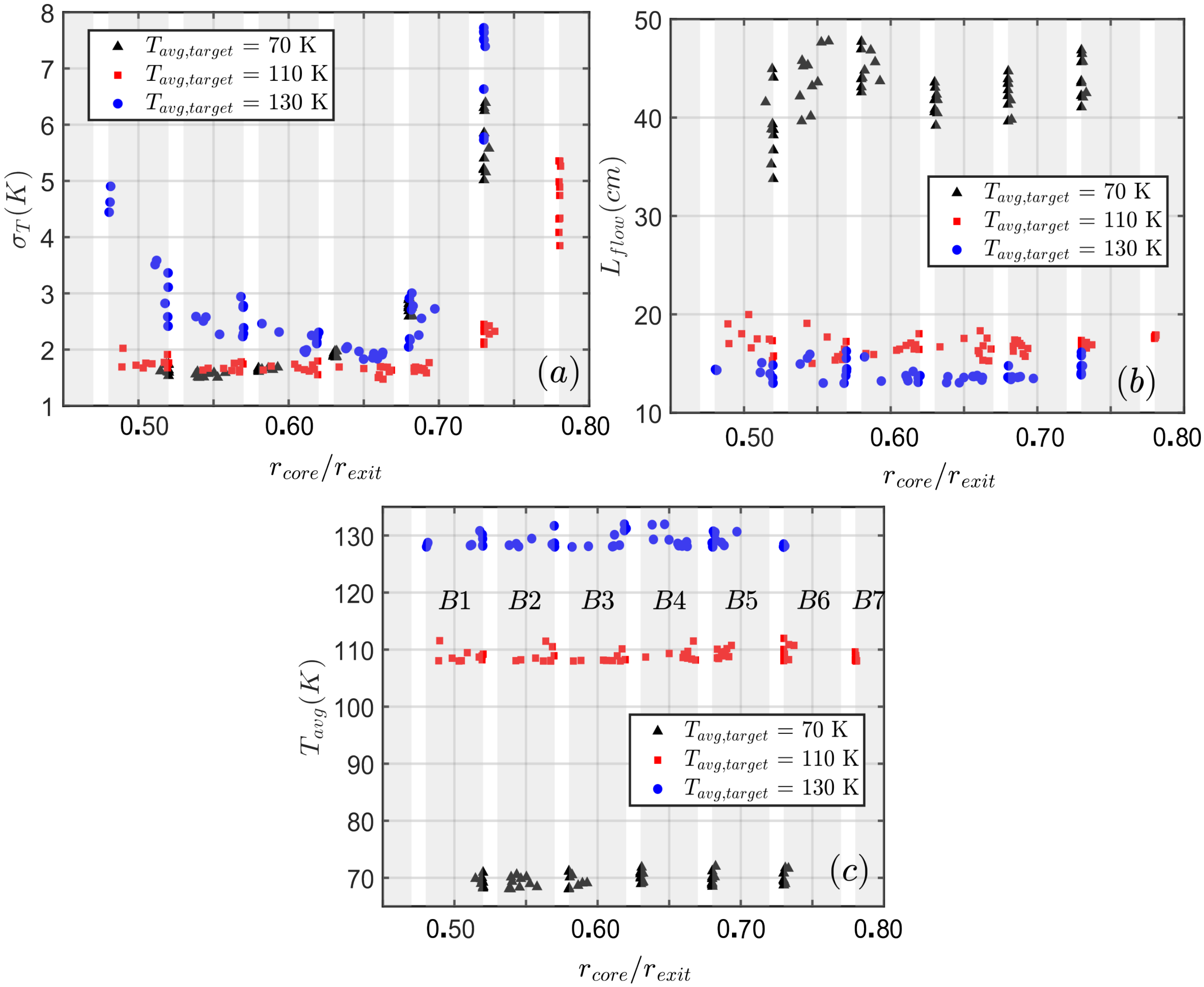

FIG. 8. Top ten optimal candidates minimizing σ_T at varying core thickness ($r_{\text{core}}/r_{\text{exit}}$) for T_{avg} = 70 K, 110 K and 130 K (a), L_{flow} versus $r_{\text{core}}/r_{\text{exit}}$ (b) and T_{avg} versus $r_{\text{core}}/r_{\text{exit}}$ (c). A bin is denoted by a gray colored stripe, where the core thickness varies by $\pm$ 0.02 around each target value of $r_{\text{core}}/r_{\text{exit}}$.

sponding FFNN predictions, LF CFD and HF CFD predictions for each nozzle shown in Table III. The nozzle lengths (L_{n}) for the $T_{\text{avg}} = 70$ K, 110 K, and 130 K cases were 111.43 mm, 60.78 mm, and 37.42 mm, respectively. The corresponding outlet radii were 16.55 mm, 8.62 mm, and 6.87 mm, respectively. The resulting area ratios (A/A^*) for $T_{\text{avg}} = 70$ K, 110 K, and 130 K were 19.57, 5.71, and 3.82, respectively. The nozzle contours across all temperatures resemble a bell-type nozzle, with the wall becoming nearly parallel to the streamwise direction at the exit. This behavior is expected, as bell-type nozzles improve flow efficiency and reduce the formation of shock waves in the jet[34]. The required nozzle length decreases with increasing temperature (and corresponding Mach number), meaning that higher-temperature nozzles are inherently shorter. This imposes a practical limit on the minimum temperatures achievable with a given CRESU apparatus due to mounting and throat size constraints. Higher temperature nozzles can be achieved with this framework, although with the current setup this would result in nozzles with a small exit radius, as temperature is proportional for the area ratio of the nozzle. Smaller r_{exit} and hence smaller r_{core} reduce the available probing region for kinetics, and therefore is avoided. Furthermore, as the L_{flow} (i.e. available reaction time) and r_{core} decreases at higher temperatures, designing usable nozzles for kinetics at higher temperatures would require a larger nozzle throat diameter, which in turn would necessitate increased pumping capacity or a reduced reservoir size to maintain pressures with a given CRESU system.

The optimization framework is inherently flexible, with the ability to accommodate alternative surrogate models and adaptive sampling strategies without modification to the un-

TABLE III. Location of the optimal ($\mathbf{x}^*$) for each value of $T_{\mathrm{avg,target}}$ designed and performance metrics of the optimized nozzle between the FFNN prediction, LF CFD validation, HF CFD validation for the nozzles at $T_{\mathrm{avg,target}}$ = 70 K, 110 K, and 130 K.

Model	σ_T (K)	T_{avg} (K)	L_{flow} (cm)	r_{core} (mm)
$T_{avg,target} = 70$ K, $P_{\mathrm{res}} = 4981$ Pa, $P_{\mathrm{chm}} = 30.4$ Pa; $\mathbf{x}^*$ = [1.000, 0.921, 0.995, 0.668, 0.998, 0.045, 0.219, 0.492, 0.448]				
FFNN	1.88	70.97	41.79	10.42
LF CFD	0.99	71.65	43.39	10.30
HF CFD	1.17	71.63	45.74	10.48
$T_{avg,target} = 110$ K, $P_{\mathrm{res}} = 4835$ Pa, $P_{\mathrm{chm}} = 150$ Pa; $\mathbf{x}^*$ = [0.605, 0.992, 0.987, 0.404, 0.990, 0.244, 0.325, 0.426, 0.464]				
FFNN	1.67	109.58	17.33	5.91
LF CFD	1.61	109.90	18.04	5.92
HF CFD	1.48	109.51	20.09	6.19
$T_{avg,target} = 130$ K, $P_{\mathrm{res}} = 2764$ Pa, $P_{\mathrm{chm}} = 145$ Pa; $\mathbf{x}^*$ = [0.593, 0.185, 0.833, 0.349, 0.818, 0.673, 0.863, 0.301, 0.037]				
FFNN	2.55	128.26	13.37	4.73
LF CFD	1.48	127.60	14.23	4.84
HF CFD	1.90	127.10	16.38	5.00

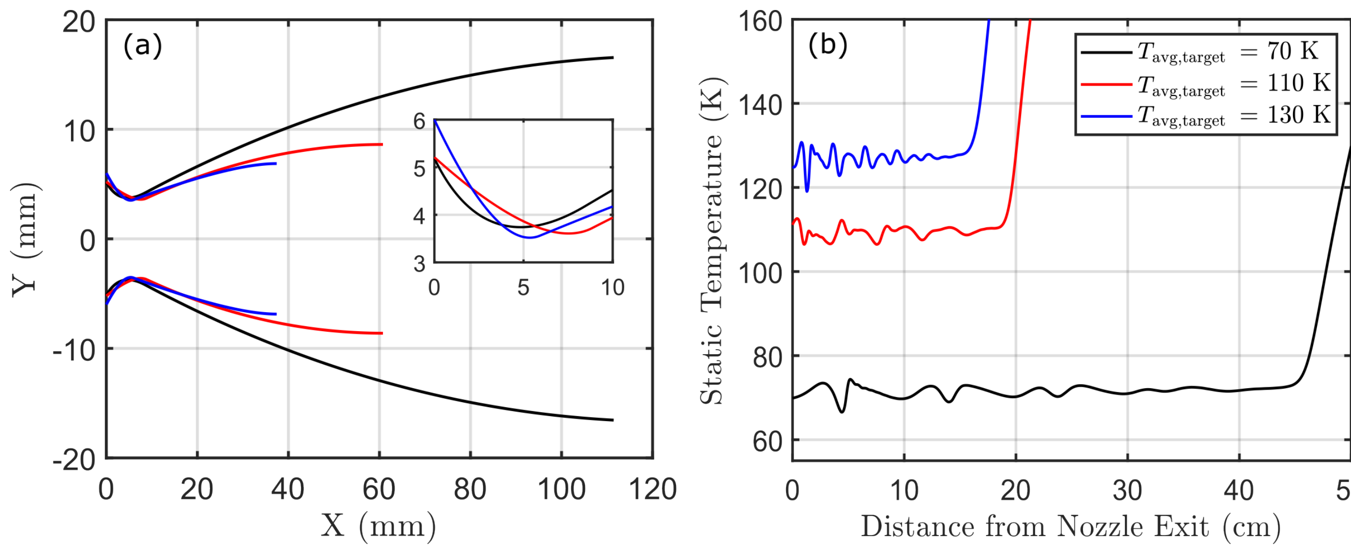

FIG. 9. Optimal nozzle designs for $T_{\mathrm{avg,target}}$ = 70 K, 110 K and 130 K with a close-up insert of the diverging section of each nozzle profile (a) and axial static temperature profile (HF CFD prediction) from the nozzle exit for each temperature (b). The colormap is valid for both figures. Note that the ordinate-to-abscissa ratio for (a) is 3 and the insert is 3.333.

derlying workflow. While the framework can be readily applied to other CRESU apparatuses through suitable redefinition of the design space and constraints, its computational cost remains non-negligible ($\approx$ 900 hours). Continued methodological refinements, including adaptive sampling strategies such as constrained expected improvement, are being pursued to enhance efficiency and facilitate wider use across CRESU facilities, with minimal computational cost.

C. Experimental Validation

The three optimized nozzles ($T_{avg,target} = 70$ K, 110 K, and 130 K) were CNC machined from aluminum or steel using a five-axis process, with a manufacturing tolerance of $\pm$0.1 mm. The nozzles were characterized using the CRESU apparatus described in Section II, where both axial and radial flow profiles were measured using Pitot tube techniques. These measurements were compared directly with HF CFD predictions. Nitrogen was used as the bath gas in both the simulations and experiments. A comparison between the HF CFD and experimentally measured reservoir (P_{res}) and chamber (P_{chm}) pressures is presented in Table IV, showing a maximum absolute percentage difference of 1.1%. This confirms that the HF CFD solution is validated through agreement with the experimental data.

Figure 10 shows the axial static temperature profiles from the experiment, HF CFD and LF CFD predictions. Note that the experimental results shown do not include the flow past the breakdown of the isentropic core (Rayleigh-Pitot is invalid, re-

TABLE IV. Reservoir and chamber pressure differences obtained from CFD and experiments (Exp). The experimental pressure were averaged across 50 runs. NPR relates to the nozzle pressure ratio, where NPR = $P_{\text{res}}/P_{\text{chm}}$. Abs(%) relates to the absolute percentage difference between the experimental and CFD optimized pressures.

	P_{res} (Pa)			P_{chm} (Pa)			NPR	
Case	CFD	Exp	Abs (%)	CFD	Exp	Abs (%)	CFD	Exp
T_{avg} = 70 K	4981	4950	0.62	30.40	30.46	0.20	163.85	162.51
T_{avg} = 110 K	4835	4809	0.54	150.00	151.67	1.10	32.23	31.70
T_{avg} = 130 K	2764	2771	0.25	145.00	145.67	0.46	19.06	19.02

sulting in a nonsensical reduction in calculated temperature), more information on why this occurs is discussed in Driver et al.[32]. The CFD predictions across the flow axis are in close agreement with the experimental measurements, showing the ability of the RANS CFD approach in resolving a supersonic flow. Note that the experimental uncertainty at each location across the jet ($\pm$ 1.5 K) is approximated based on Lucas et al.[9] and may vary depending on the Mach number. This is because only averaged data is retained during the characterization process, and the majority fo CRESU studies only report the averaged value without error metrics. It should be noted that including error bars could be used to aid in comparing measurement accuracy across the field.

A comparison between the jet properties across the axis of the jet for the LF CFD, HF CFD and experimental results of each tested nozzle is shown in Table V. The HF CFD predictions show close agreement in relation to T_{avg}, σ_T, r_{core}, M_{avg} with the experimental temperature measurements across all nozzles tested in this study. Note that the typical discrepencies between CFD and experimental jet properties are similar to those found in a previous study comparing RANS and experimental Pitot tube results[32]. The LF CFD predictions are also presented, demonstrating that the lower mesh density is able to robustly capture the primary flow quantities when compared to a fully high-fidelity optimization approach. The manufactured CNC nozzles in this study were not characterized using surface measurement techniques. Variations from the CAD geometry, particularly in the area ratio, may lead to differences in the jet temperature during experiments, as the parts are relatively small in diameter. Therefore small tolerances or variability from the intended design can have a significant effect, especially at higher temperatures (more sensitive to area ratio), changing the shock dynamics and temperature of the wake past the nozzle exit.

For the flow length in the T_{avg} = 70 K case, the experimental flow length cannot be defined as the Pitot tube can only traverse 50 cm from the nozzle exit due to the length of this nozzle. The flow lengths for T_{avg} = 110 K and 130 K are both approximately 5 cm shorter than the HF CFD predictions. The nozzle exit temperatures are also higher for these cases, and the reduction in flow length may be attributed to increased turbulence production throughout the reservoir in the experiments, which is not captured by the idealized steady-state RANS model. A more detailed study is required to come to a definitive conclusion on the exact reasoning behind this trend. The isentropic core diameter reduces across the jet due to viscous shearing, when the Pitot tube diameter is a similar size to the isentropic core, shock losses can invalidate the temperature of the jet, hence the nonphysical reduction in temperature across the jet and outside the core in the experimental results.

A higher-fidelity model, such as LES or a 3D study with all flow features (asymmetric outlet and inlet pipes to the reservoir) may be required to accurately capture these unsteady flow effects at higher temperatures. Especially shock wave interactions with the shear layer that is present past the nozzle exit, where LES has shown to accurately resolve shock location and turbulent production over traditional RANS models for supersonic compressible flow. Nevertheless, the present results demonstrate that a steady RANS framework, combined with adaptive FFNN surrogate modeling, is capable of accurately predicting the mean flow structure and key trends in supersonic nozzle flows at conditions relevant to the CRESU method. Overall, the agreement between CFD and experiment confirms that the observed coupling between r_{core}, L_{flow} and σ_T is physically realized in the flow, rather than being an artifact of the optimization framework. This validates the identification of a constrained operating regime governing σ_T and usable core extent in low-temperature supersonic jets.

A comparison of the 2D axisymmetric static temperature fields across the jet for both the LF CFD predictions, HF CFD predictions and the experimental measurements is shown in Figure 11. Panels (a), (b), and (c) correspond to the LF CFD predictions and (d), (e) and (f) are the HF CFD predictions for the 130 K, 110 K, and 70 K nozzles, respectively, while panels (g), (h), and (i) show the corresponding experimental results. Both the 130 K and 110 K CFD predictions capture the shear layer growth and reduction of core diameter across the length of the jet up to just before the flow breakdown point seen in the experiments (9 cm for the 130 K nozzle and 15 cm for the 110 K nozzle). Near the end of the core, the experimental jet appears much more diffuse. This may be attributed to the upstream reservoir turbulence, or the the size of the Pitot tube relative to the core flow (5 mm inlet diameter), which could cause the measured impact pressure to be partially averaged with the shear layer introducing additional shock-related losses. This may be why there is not a distinct core towards the end of the flow. For the 70 K nozzle, the RANS model predicts the boundary-layer thickness at the nozzle exit accurately. However, the experimental results show that the core decays significantly more slowly than the RANS prediction. This slower decay is actually favorable for kinetics studies, as it increases the available hydrodynamic time for reaction processes.

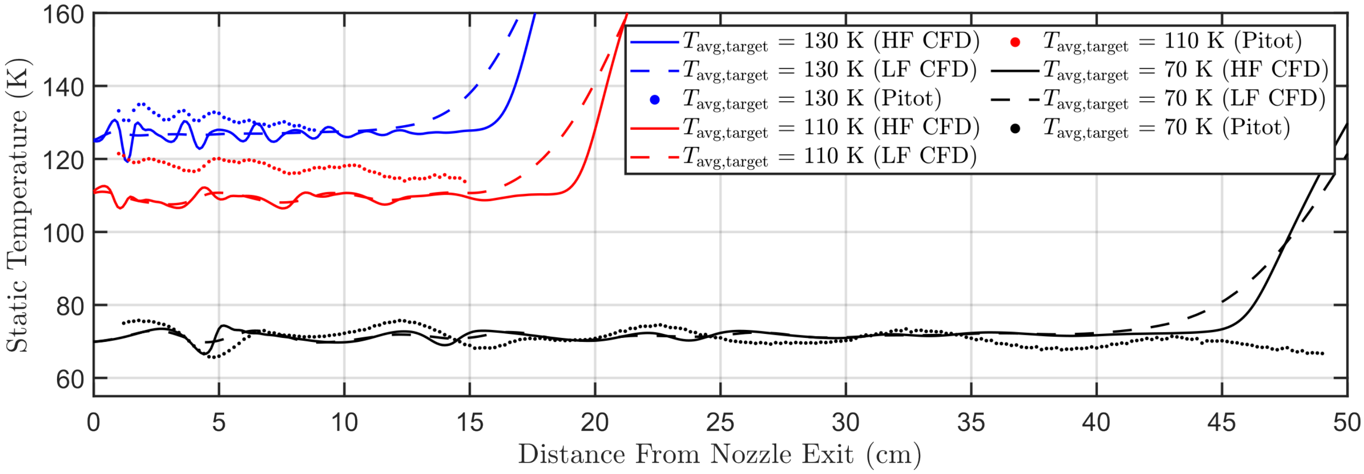

FIG. 10. Comparison of axial static temperature between the HF CFD predictions (solid lines), LF CFD predictions (dashed lines) and experimental Pitot tube characterization (markers) for the nozzles at $T_{avg,target}$ = 70 K, 110 K and 130 K. The experimental results at each Pitot tube location are averaged over 50 repeats. The estimated temperature uncertainty at any point across the jet is $\pm$1.5 K[9].

TABLE V. Comparison of main jet quantities between HF CFD predictions and experimental Pitot tube characterization results across the axis of the flow.

-	σ_T (K) [a]	T_{avg} (K)	M_{avg} (-)	L_{flow} (cm) [b]	r_{core} (mm)
70 K HF CFD	1.17	71.63	3.94	45.74	10.50
70 K Experiment	2	71	4.0	>50	10+
110 K HF CFD	1.48	109.51	2.90	20.09	6.19
110 K Experiment	2	117	2.7	15	6
130 K HF CFD	1.90	127.10	2.56	16.38	5.00
130 K Experiment	2	131	2.5	9	4

[a] The σ_T would be close to $\approx$ 1 K if a shorter flow length were chosen. The difference in temperature between successive shocks is $<$ 4 K for all nozzles in the experiments

[b] This value is taken from the first experimental data point, not the nozzle exit, and is approximated as the experiments are in 2 mm intervals.

The experimental temperature contours without processing would show a non-physical reduction in static temperature outside the core, as the Rayleigh–Pitot equations are invalid, due to idealized assumptions, such as inviscid, irrotational flow. One potential way of recovering the correct jet temperature has been proposed, which consists of linearly transforming the experimentally obtained freestream temperature to ambient conditions (293 K), a behavior which is predicted by the CFD calculations. A linear transformation was used as the temperature rises back to ambient in an approximately linear fashion through the boundary layer after the flow reaches the end of the core, shown in Figure 10. The linear transformation of the experimental results for each nozzle is shown in Figure 11h, 11i and 11j. The linear transformation of the experimental results can more accurately predict the boundary layer temperature surrounding the isentropic core, and can be useful in chemical kinetic studies. More information on the implementation of the transformation and raw experimental data can be found in the supplementary material.

Overall, these results demonstrate that the proposed framework, combining surrogate-based optimization with steady-state RANS modeling, is effective for nozzle design and is supported by consistent trends across both CFD and experimental measurements. The framework developed here can target longer flow lengths at high temperatures by adjusting the $L_{flow,target}$ constraint. Increasing L_{flow} generally increases σ_T, but it provides far more flexibility in nozzle design than the traditional MOC approaches typically used in CRESU over the past decade. Note that these nozzles have not been compared directly to MOC nozzles, although they theoretically perform similarly to the best nozzles seen across the literature (shown in Figure 1).

Upwards of 75% improvement in σ_T is seen with the designed nozzles in this work compared to legacy MOC nozzle designs used at the University of Leeds and University of Birmingham, especially at higher temperatures[9,62,63]. Note that the nozzles shown in Figure 1 represent the best designs achieved using the MOC, which typically requires many iterative refinement cycles. In contrast, the approach described in Section III C requires only a single design loop, as the CFD predictions show good agreement with experimental measurements, thereby significantly reducing both manufacturing and experimental costs. Although the surrogate model requires approximately 35 days to generate, it is worth noting that using the current MOC approach can take weeks with iterative testing using 3D printing, but the surrogate approach greatly

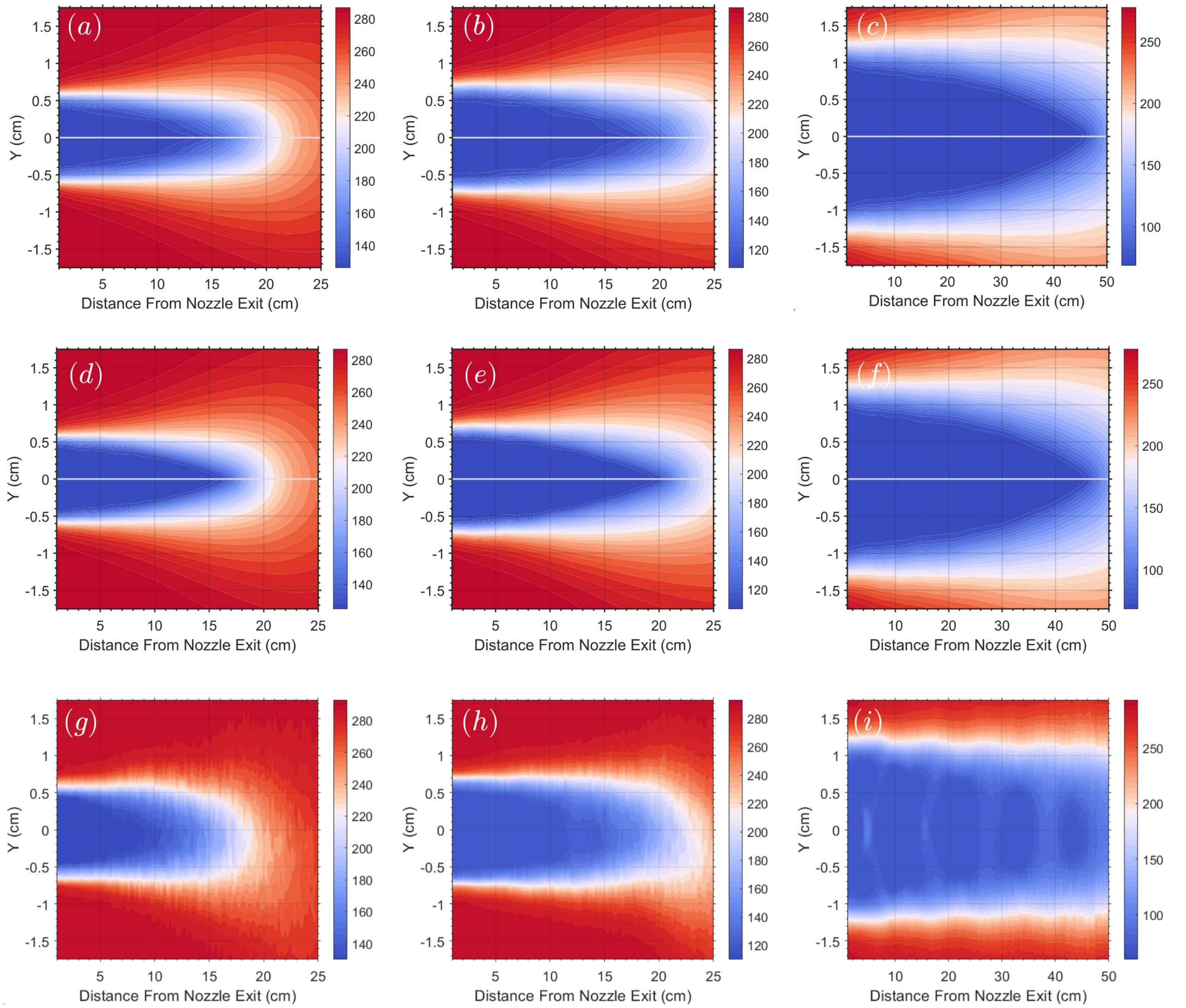

FIG. 11. Static temperature contours where (a) and (b) and (c) is the LF CFD 130 K, 110 K and 70 K results respectively, (d), (e) and (f) are the 130 K, 110 K and 70 K LF CFD results respectively, and (g), (h) and (i) are the experimental measurements for the 130 K, 110 K and 70 K nozzles respectively. Note that the experimental results have been linearly transformed to match the colourmap of the CFD results as the Rayleigh-Pitot equation is invalid outside the core region. More information on this transformation can be found in supplementary material.

reduces person-time, experimental cost, and waste as designs are predictive. Furthermore, this framework is capable of designing nozzles that generate a profile for desired flow conditions and temperatures for kinetics studies. Once the surrogate data is available, design constraints, such as operating pressure or flow length, can be adjusted with ease, and an optimal nozzle configuration can be obtained in under three hours using the FFNN surrogate. The optimal nozzle can then be passed through the ACRE framework for validation and to aid in kinetic studies. Additive manufacturing (AM) can be used to rapidly produce and test nozzles, and then can be machined once performance is established using AM techniques.

IV. CONCLUSION

This work has investigated the design and performance of low-temperature de Laval nozzles for CRESU applications, combining CFD-based optimization with experimental validation. The results reveal a fundamental trade-off governing supersonic jet formation, in which the thickness of the r_{core} controls the minimum value of σ_T.

A critical core thickness is identified, beyond which increasing core momentum amplifies shockwave magnitude across the jet. At lower core thickness values, the supersonic jet has minimal flow oscillations, but the associated boundary layer growth reduces the effective uniform core region available for kinetic measurements. This establishes a constrained operating regime, where σ_T and r_{core}, cannot be simultaneously minimized and maximized respectively, but must instead be balanced. The dependence of this trade-off on Mach number (and jet temperature) is also demonstrated, with the maximum attainable core thickness decreasing at higher Mach numbers due to increased nozzle lengths, which in turn enhance boundary-layer growth along the nozzle wall at the pressures tested.

The optimization framework was applied to the design of three nozzles operating at 70 K, 110 K, and 130 K, demonstrating its capability to explore a large and flexible design space encompassing multiple geometric parameters and optimization constraints. This breadth enabled systematic investigation of the influence of isentropic core thickness, reveals it as a critical optimization constraint. When this parameter is not explicitly constrained, the optimizer tends to converge toward designs with artificially reduced r_{core} values, for which σ_T is typically minimized. The resulting optimal nozzle geometries and operating pressures were manufactured and experimentally validated, showing good agreement between CFD predictions and experimental measurements. The σ_T and T_{avg} obtained using the Pitot tube method were within 1 K and 5 – 10 K of the RANS CFD predictions respectively. The numerical framework used in this study can be found at github.com/sc1dr/KOSMOS, with ongoing development for a more robust optimization code based on Bayesian optimization set to be released in the near future for use across CRESU groups and beyond.

While the present study employs surrogate-assisted optimization as a design tool, its primary contribution lies in revealing the fluid-mechanical constraints governing nozzle performance. More broadly, the approach provides a framework for systematically exploring the interaction between geometry, operating conditions, jet temperature, standard deviation of temperature and flow length in supersonic nozzle flows. These findings have direct implications for the design of CRESU systems and establish a basis for future optimization studies that require flow conditioning of a supersonic jet. These results confirm both the predictive accuracy of the general framework and a demonstration of its value as a versatile design tool for the CRESU community.

SUPPLEMENTARY MATERIAL

The supplementary material provides detailed supporting information for the study. This includes results from a series of lower-dimensional parametric investigations that informed and guided the final nine-dimensional (9D) optimization study presented in the main paper. Additional mathematical formulations are provided for key components of the design optimization framework, including surrogate modeling via Kriging, the construction of Optimal Latin Hypercube sampling strategies, and the definition and implementation of objective functions. The supplementary material also documents the data processing workflow, detailing the transformation of raw experimental measurements into a form suitable for direct comparison with computational fluid dynamics (CFD) results.

ACKNOWLEDGMENTS

This work is part of a project that has received funding from the European Research Council (ERC) under the European Union's Horizon 2020 research and innovation program (Grant agreement No. 948525). This work was also supported by the EPSRC Centre for Doctoral Training in Fluid Dynamics (EP/S022732/1). Computational work was undertaken on ARC4 and AIRE, part of the High-Performance Computing facilities at the University of Leeds, UK and University of Birmingham. See https://arcdocs.leeds.ac.uk and https://www.birmingham.ac.uk/bear for more details.

DATA AVAILABILITY STATEMENT

The optimization data that supports the finding of this study can be found at github.com/sc1dr/KOSMOS, whilst the computational fluid dynamics framework used can be found at github.com/sc1dr/ACRE.

REFERENCES

[1] W. R. Stockwell, C. V. Lawson, E. Saunders, and W. S. Goliff, "A review of tropospheric atmospheric chemistry and gas-phase chemical mechanisms for air quality modeling," Atmosphere **3**, 1–32 (2011).

[2] L. Biennier, H. Sabbah, V. Chandrasekaran, S. J. Klippenstein, I. R. Sims, and B. R. Rowe, "Insights into the role of polycyclic aromatic hydrocarbon condensation in haze formation in jupiter's atmosphere," Astronomy & Astrophysics **532**, A40 (2011).

[3] E. Jiménez, M. Antiñolo, B. Ballesteros, A. Canosa, and J. Albaladejo, "First evidence of the dramatic enhancement of the reactivity of methyl formate ($HC(O)OCH_3$) with OH at temperatures of the interstellar medium: a gas-phase kinetic study between 22 K and 64 K," Physical Chemistry Chemical Physics **18**, 2183–2191 (2016).

[4] A. Canosa, A. J. Ocaña, M. Antiñolo, B. Ballesteros, E. Jiménez, and J. Albaladejo, "Design and testing of temperature tunable de laval nozzles for applications in gas-phase reaction kinetics," Experiments in Fluids **57**, 152 (2016).

[5] B. Joalland, N. Jamal-Eddine, D. Papanastasiou, A. Lekkas, S. Carles, and L. Biennier, "A mass-selective ion transfer line coupled with a uniform supersonic flow for studying ion–molecule reactions at low temperatures," The Journal of Chemical Physics **150**, 164201 (2019).

[6] C. Sleiman, G. El Dib, D. Talbi, and A. Canosa, "Gas phase reactivity of the CN radical with methyl amines at low temperatures (23–297 k): A combined experimental and theoretical investigation," ACS Earth and Space Chemistry **2**, 1047–1057 (2018).

[7] N. Suas-David, S. Thawoos, and A. G. Suits, "A uniform flow–cavity ring-down spectrometer (UF-CRDS): A new setup for spectroscopy and kinetics at low temperature," The Journal of Chemical Physics **151**, 244202 (2019).

[8] C. Berteloite, M. Lara, A. Bergeat, S. D. Le Picard, F. Dayou, K. M. Hickson, A. Canosa, C. Naulin, J.-M. Launay, I. R. Sims, and M. Costes, "Kinetics and dynamics of the S ($^1D_2$) + $H_2 \rightarrow$ SH + H reaction at very low temperatures and collision energies," Physical Review Letters **105**, 203201 (2010).

[9] D. I. Lucas, T. Guillaume, D. E. Heard, and J. H. Lehman, "Design and implementation of a new apparatus for astrochemistry: Kinetic measurements of the CH + OCS reaction and frequency comb spectroscopy in a cold uniform supersonic flow," The Journal of Chemical Physics (2024).

[10]S. E. Taylor, A. Goddard, M. A. Blitz, P. A. Cleary, and D. E. Heard, "Pulsed laval nozzle study of the kinetics of OH with unsaturated hydrocarbons at very low temperatures," Phys. Chem. Chem. Phys. **10**, 422–437 (2008).

[11]E. Herbst, "Chemistry in the interstellar medium," Annual Review of Physical Chemistry **46**, 27–54 (1995), publisher: Annual Reviews Type: Journal Article.

[12]A. G. G. M. Tielens, "The molecular universe," Reviews of Modern Physics **85**, 1021–1081 (2013).

[13]B. A. McGuire, "2021 census of interstellar, circumstellar, extragalactic, protoplanetary disk, and exoplanetary molecules," The Astrophysical Journal Supplement Series **259**, 30 (2022).

[14]B. R. Rowe, A. Canosa, and D. E. Heard, *Uniform Supersonic Flows in Chemical Physics* (WORLD SCIENTIFIC (EUROPE), 2022) https://www.worldscientific.com/doi/pdf/10.1142/q0324.

[15]A. Potapov, A. Canosa, E. Jiménez, and B. Rowe, "Uniform supersonic chemical reactors: 30 years of astrochemical history and future challenges," Angewandte Chemie International Edition **56**, 8618–8640 (2017).

[16]O. Abdelkader Khedaoui, *Improving the sensitivity of mm-wave rotational spectroscopy in uniform supersonic flows for laboratory astrophysics applications*, Ph.D. thesis, Université de Rennes (2022).

[17]S. Thawoos, N. Suas-David, R. M. Gurusinghe, M. Edlin, A. Behzadfar, J. Lang, and A. G. Suits, "Low temperature reaction kinetics inside an extended laval nozzle: REMPI characterization and detection by broadband rotational spectroscopy," The Journal of Chemical Physics **159**, 214201 (2023).

[18]A. J. Ocaña, S. Blázquez, A. Potapov, B. Ballesteros, A. Canosa, M. Antiñolo, L. Vereecken, J. Albaladejo, and E. Jiménez, "Gas-phase reactivity of CH $_3$OH toward OH at interstellar temperatures (11.7–177.5 K): experimental and theoretical study," Physical Chemistry Chemical Physics **21**, 6942–6957 (2019).

[19]A. Mortada, S. Carles, S. Demes, B. Joalland, F. Lique, A. Benidar, P. Lavvas, and L. Biennier, "Kinetics and branching for the reactions of N_2^+ with C_3 H_4 isomers at low temperatures and implications for titan's atmosphere," ACS Earth and Space Chemistry **6**, 1227–1238 (2022).

[20]R. L. Caravan, *Low Temperature Kinetic Studies using a Pulsed Laval Nozzle Apparatus*, Ph.D. thesis, University of Leeds (2015).

[21]G. Dupeyrat, J. B. Marquette, and B. R. Rowe, "Design and testing of axisymmetric nozzles for ion-molecule reaction studies between 20 K and 160 K," The Physics of Fluids **28**, 1273–1279 (1985).

[22]D. B. Atkinson and M. A. Smith, "Design and characterisation of pulsed uniform supersonic nozzles," Review of Scientific Instruments **66**, 4434–4446 (1995).

[23]O. Durif, "Design of de laval nozzles for gas-phase molecular studies in uniform supersonic flow," Physics of Fluids **34**, 013605 (2022).

[24]B. R. Rowe, G. Dupeyrat, J. B. Marquette, and P. Gaucherel, "Study of the reactions $N_2 + 2N_2 \rightarrow N_4 + N_2$ and $O_2 + 2O_2 \rightarrow O_4 + O_2$ from 20 to 160 K by the CRESU technique," The Journal of Chemical Physics **80**, 4915–4921 (1984).

[25]B. Schläppi, J. H. Litman, J. J. Ferreiro, D. Stapfer, and R. Signorell, "A pulsed uniform laval expansion coupled with single photon ionization and mass spectrometric detection for the study of large molecular aggregates," Physical Chemistry Chemical Physics **17**, 25761–25771 (2015).

[26]E. Jiménez, B. Ballesteros, A. Canosa, T. M. Townsend, F. J. Maigler, V. Napal, B. R. Rowe, and J. Albaladejo, "Development of a pulsed uniform supersonic gas expansion system based on an aerodynamic chopper for gas phase reaction kinetic studies at ultra-low temperatures," Review of Scientific Instruments **86**, 045108 (2015).

[27]D. Munday, E. Gutmark, J. Liu, and K. Kailasanath, "Flow structure and acoustics of supersonic jets from conical convergent-divergent nozzles," Physics of Fluids **23**, 116102 (2011).

[28]S. M. Mousavi and E. Roohi, "Large eddy simulation of shock train in a convergent-divergent nozzle," International Journal of Modern Physics C **25** (2014), 10.1142/S012918311450003X.

[29]A. Balabel, A. Hegab, M. Nasr, and S. M. El-Behery, "Assessment of turbulence modeling for gas flow in two-dimensional convergent–divergent rocket nozzle," Applied Mathematical Modelling **35**, 3408–3422 (2011).

[30]G. Besagni and F. Inzoli, "Computational fluid-dynamics modeling of supersonic ejectors: Screening of turbulence modeling approaches," Applied Thermal Engineering **117**, 122–144 (2017).

[31]K. Bhide and S. Abdallah, "High-order accurate numerical simulation of supersonic flow using RANS and LES guided by turbulence anisotropy," Fluids **7**, 385 (2022).

[32]L. Driver, K. Douglas, D. I. Lucas, T. Guillaume, J. H. Lehman, N. Kapur, D. E. Heard, and G. N. De Boer, "Developing a predictive model for low-temperature laval nozzles with applications in chemical kinetics," Physics of Fluids **36**, 076128 (2024).

[33]L. H. D. Li, K. M. Douglas, F. Hall, A. Kirker, L. Driver, G. N. de Boer, N. Kapur, J. H. Lehman, M. A. Blitz, and D. E. Heard, "Experimental and theoretical study of the kinetics of dimerization of ammonia at low temperatures," The Journal of Physical Chemistry A **129**, 6289–6305 (2025), pMID: 40590847, https://doi.org/10.1021/acs.jpca.5c03008.

[34]S. Khare and U. Saha, "Rocket nozzles: 75 years of research and development," Sadhana **46** (2021).

[35]C. Fujio and H. Ogawa, "Physical insight into axisymmetric scramjet intake design via multi-objective design optimization using surrogate-assisted evolutionary algorithms," Aerospace Science and Technology **113**, 106676 (2021).

[36]H. Ogawa and R. R. Boyce, "Nozzle design optimization for axisymmetric scramjets by using surrogate-assisted evolutionary algorithms," Journal of Propulsion and Power **28**, 1324–1338 (2012).

[37]M. Yumuşak and S. Eyi, "Design optimization of rocket nozzles in chemically reacting flows," Computers & Fluids **65**, 25–34 (2012).

[38]T. Fernandes, A. Souza, and F. Afonso, "A shape design optimization methodology based on the method of characteristics for rocket nozzles," CEAS Space Journal **15**, 867–879 (2023).

[39]M. Yumuşak, "Analysis and design optimization of solid rocket motors in viscous flows," Computers & Fluids **75**, 22–34 (2013).

[40]X. Q. Xing and M. Damodaran, "Design of three-dimensional nozzle shape using NURBS, CFD and hybrid optimization strategies," AIAA (2004).

[41]L. Bo, Q. Wang, and H. Hu, "Collaborative optimization of two-dimensional convergent divergent exhaust system based on kriging model," Physics of Fluids **36**, 076117 (2024).

[42]L. Alonso, M. Garrido, and P. Poza, "An optimisation method for the cold-spray process: On the nozzle geometry," Materials & Design **214**, 110387 (2022).

[43]C. Wang, Q. Eri, Y. Wang, B. Kong, and W. Ding, "Multi-objective aerodynamic optimization of an axisymmetric variable-geometry inlet with a mach 5 design point," Aerospace Science and Technology **136**, 108189 (2023).

[44]P. Toniato, D. E. Gildfind, P. A. Jacobs, and R. G. Morgan, "Expansion tube nozzle design using a parallel simplex algorithm," Shock Waves **30**, 185–199 (2020).

[45]M. Matsunaga, C. Fujio, H. Ogawa, Y. Higa, and T. Handa, "Nozzle design optimization for supersonic wind tunnel by using surrogate-assisted evolutionary algorithms," Aerospace Science and Technology **130**, 107879 (2022).

[46]K. Kamali, P. Gaetani, G. Persico, and A. Romei, "CFD-based shape optimization of flashing converging-diverging nozzles in pelton turbines for domestic carbon dioxide heat pumps including off-design conditions," Applied Thermal Engineering **257**, 124321 (2024).

[47]R. Agromayor, N. Anand, J.-D. Müller, M. Pini, and L. O. Nord, "A unified geometry parametrization method for turbomachinery blades," Computer-Aided Design **133**, 102987 (2021).

[48]L. Piegl and W. Tiller, *The NURBS Book*, Monographs in Visual Communication (Springer Berlin Heidelberg, 1996).

[49]J. Lepine, J.-Y. Trepanier, and F. Pepin, "Wing aerodynamic design using an optimized nurbs geometrical representation," in *38th Aerospace Sciences Meeting and Exhibit* (AIAA, 2012) https://arc.aiaa.org/doi/pdf/10.2514/6.2000-669.

[50]O. Abdelkader Khedaoui, *Improving the sensitivity of mm-wave rotational spectroscopy in uniform supersonic flows for laboratory astrophysics applications*, Theses, Université de Rennes (2022).

[51]N. Georgiadis and D. Papamoschou, "Computational Investigations of High-Speed Dual Stream Jets," in *9th AIAA/CEAS Aeroacoustics Conference and Exhibit* (American Institute of Aeronautics and Astronautics, Hilton Head, South Carolina, 2003).

[52]A. R. Proença, J. L. T. Lawrence, and R. H. Self, "Experimental Investigation into the Turbulence Flowfield of In-Flight Round Jets," AIAA Journal **58**, 3339–3350 (2020).

[53] M. Spink, D. Claxton, C. de Falco, and R. Vázquez, "The NURBS toolbox," `http://octave.sourceforge.net/nurbs/index.html` (2010).
[54] C. de Falco, A. Reali, and R. Vázquez, "Geopdes: A research tool for isogeometric analysis of pdes," Advances in Engineering Software **42**, 1020–1034 (2011).
[55] M. D. Morris and T. J. Mitchell, "Exploratory designs for computational experiments," Journal of Statistical Planning and Inference **43**, 381–402 (1995).
[56] J. N. Fuhg, A. Fau, and U. Nackenhorst, "State-of-the-art and comparative review of adaptive sampling methods for kriging," Archives of Computational Methods in Engineering **28**, 2689–2747 (2021).
[57] H. Liu, Y.-S. Ong, and J. Cai, "A survey of adaptive sampling for global metamodeling in support of simulation-based complex engineering design," Structural and Multidisciplinary Optimization **57**, 393–416 (2018).
[58] H. Liu, "An adaptive sampling approach for kriging metamodeling by maximizing expected prediction error," Computers and Chemical Engineering (2017).
[59] K. Crombecq, E. Laermans, and T. Dhaene, "Efficient space-filling and non-collapsing sequential design strategies for simulation-based modeling," European Journal of Operational Research **214**, 683–696 (2011).
[60] A. I. J. Forrester, A. Sóbester, and A. J. Keane, *Engineering Design via Surrogate Modelling: A Practical Guide*, 1st ed. (Wiley, 2008).
[61] P. Linstrom and W. Mallard, "NIST chemistry webbook, NIST standard reference database number 69," `https://doi.org/10.18434/T4D303` (2023), National Institute of Standards and Technology, Gaithersburg MD, 20899.
[62] K. Douglas, L. H. D. Li, C. Walsh, J. H. Lehman, M. A. Blitz, and D. E. Heard, "Experimental, theoretical, and astrochemical modelling investigation of the gas-phase reaction between the amidogen radical (NH_2) and acetaldehyde (CH_3CHO) at low temperatures," Faraday Discuss. **245**, 261–283 (2023).
[63] D. E. Heard, "Rapid acceleration of hydrogen atom abstraction reactions of oh at very low temperatures through weakly bound complexes and tunneling," Accounts of Chemical Research **51**, 2620–2627 (2018).